

Adaptive deep density approximation for Fokker-Planck equations

Kejun Tang^{a,b}, Xiaoliang Wan^c, Qifeng Liao^{a,*}

^a*School of Information Science and Technology, ShanghaiTech University, Shanghai 201210, China*

^b*Peng Cheng Laboratory, Shenzhen 518000, China*

^c*Department of Mathematics and Center for Computation and Technology, Louisiana State University, Baton Rouge 70803, USA*

Abstract

In this paper we present a novel adaptive deep density approximation strategy based on KRnet (ADDA-KR) for solving the steady-state Fokker-Planck equation. It is known that this equation typically has high-dimensional spatial variables posed on unbounded domains, which limit the application of traditional grid based numerical methods. With the Knothe-Rosenblatt rearrangement, our newly proposed flow-based generative model, called KRnet, provides a family of probability density functions to serve as effective solution candidates of the Fokker-Planck equation, which have weaker dependence on dimensionality than traditional computational approaches. To result in effective stochastic collocation points for training KRnet, we develop an adaptive sampling procedure, where samples are generated iteratively using KRnet at each iteration. In addition, we give a detailed discussion of KRnet and show that it can efficiently estimate general high-dimensional density functions. We present a general mathematical framework of ADDA-KR, validate its accuracy and demonstrate its efficiency with numerical experiments.

Keywords: density estimation; flow-based generative models; Fokker-Planck equations; deep learning.

1. Introduction

During the past few decades there has been a rapid development in numerical methods for Fokker-Planck equations. This explosion in interest has been driven by the need of assessing time evolution of probability density functions in randomly perturbed dynamical systems, which are widely used in physical and biological modeling [1, 2, 3]. It is known that there exist two main challenges for efficiently solving the Fokker-Planck equations: the spatial variable can be high-dimensional, which causes difficulties in applying grid based numerical methods, e.g. finite element methods [4, 5]; the original spatial domain is typically unbounded, and it is challenging to derive a well-posed boundary condition for a bounded computational domain. To alleviate these difficulties, new numerical methods based on deep learning currently gain a lot of interests [6, 7], and this paper is devoted to deep learning for the Fokker-Planck equations.

Deep learning methods for partial differential equations (PDEs) are under active development. In [8, 9], a deep Ritz method is proposed based on variational methods. In [10, 11, 12, 13], physics-informed neural networks are developed through infusing PDEs into networks. A deep Galerkin method is proposed in [14]. Bayesian deep convolutional

*Corresponding author

Email addresses: tangkj@shanghaitech.edu.cn (Kejun Tang), xlwan@lsu.edu (Xiaoliang Wan), liaoqf@shanghaitech.edu.cn (Qifeng Liao)

encoder-decoder networks for PDEs with high-dimensional random inputs are developed in [15, 16]. Deep learning strategies are also introduced to discover physical laws [17, 18]. In addition, efficient deep learning methods based on domain decomposition are studied in [19, 20, 21, 22, 23, 24], and deep neural network methods for complex geometries and irregular domains are proposed in [25, 26]. A main idea of deep learning methods for PDEs is to reformulate a PDE problem as an optimization problem and train deep neural networks through minimizing the corresponding loss functional. In these methods, stochastic collocation points are required to estimate the loss functional. We note that the stochastic collocation points herein are for the spatial variable, while stochastic collocation for PDEs with random inputs (especially for parameters) are discussed in detail in [27, 28, 29, 30, 31, 32, 33]. To result in an efficient deep learning strategy for PDEs, properly choosing the collocation points are crucial. In our recent work [19], a hierarchical sampling procedure are proposed based on domain decomposition iterations, while it focuses on low-dimensional problems. As the spatial variable of the Fokker-Planck equation can be high-dimensional, it remains an open challenging problem to generate its effective collocation points, and we develop a novel efficient adaptive sampling procedure in this work.

As the solution of the Fokker-Planck equation is a probability density function, solving this problem can also be considered as a density estimation problem. It is known that density estimation is a central topic in unsupervised learning, and it still remains an open challenge for high-dimensional density estimation [34]. Recently, two kinds of deep learning models have shown great promise for estimating high-dimensional density functions, which include the flow-based generative model [35, 36] and the neural ordinary differential equation model [37, 38]. In this work, we focus on the flow-based generative model, which is to construct invertible mappings from a given prior distribution to the data under consideration and build explicit probability density functions using the change of variables formula. The invertible mapping can be viewed as a special case of the Knothe-Rosenblatt (KR) rearrangement [39], which constructs mappings through triangular structures. In particular, we propose a novel invertible block-triangular mapping, which gives a generalization for the standard flow-based generative model. In addition, coupling flow-based generative models and reduced-order models into an importance sampling estimator is studied in [40]. We note that there are a lot of generative models which can efficiently generate samples of distributions under consideration but could not explicitly give the corresponding density functions, e.g., generative adversarial networks (GANs) [41] and the variational autoencoder (VAE) [42].

In this work, we propose a novel adaptive deep density approximation method based on KRnet (ADDA-KR) for solving Fokker-Planck equations. First, our novel invertible mapping called KRnet is discussed in detail in this work, where new layers are introduced to improve the robustness and effectiveness of flow-based generative models. After that, this new flow-based generative model is used to construct solutions of the Fokker-Planck equation. Since the flow-based generative model can represent a family of probability density functions, vanishing boundary and normality conditions are satisfied naturally. Like other deep learning algorithms for solving PDEs, our method is also meshfree, which curbs the difficulty of curse of dimensionality. Our KRnet can also efficiently provide samples on the spatial domain, which can be served as stochastic collocation points. Our novel ADDA-KR approach can then be outlined as repeating the following two steps: computing a current KRnet to approximate the solution of the Fokker-

Planck equation, and using this KRnet to generate collocation points for the next iteration. To summarize, the main contributions of this work are two-fold: first, our new KRnet provides an effective invertible mapping for flow-based generative models; second, our ADDA-KR approach gives an efficient adaptive procedure for solving the stationary Fokker-Planck equation. The rest of the paper is organized as follows. In the next section, the Fokker-Planck equations and the problem setting are introduced. The structure of flow-based generative models is presented in section 3. Our new KRnet are introduced in section 4. In section 5, our novel adaptive deep density approximation approach for the Fokker-Planck equation is presented. In section 6, we demonstrate the efficiency of our adaptive sampling approach with numerical experiments. Finally section 7 concludes the paper.

2. Problem setup

Consider the state X_t modeled by the following stochastic differential equation

$$dX_t = \boldsymbol{\mu}(X_t, t)dt + \mathbf{G}(X_t, t)d\mathbf{w}_t, \quad (1)$$

where $\boldsymbol{\mu} = [\mu_1, \dots, \mu_d]^\top$ is a vector field, $\mathbf{G}(X_t, t) \in \mathbb{R}^{d \times d}$ is a matrix-valued function and \mathbf{w}_t is a d -dimensional standard Wiener process. The Fokker-Planck equation, which describes the probability density function of X_t , is

$$\begin{aligned} \frac{\partial p(\mathbf{x}, t)}{\partial t} = \mathcal{L}p(\mathbf{x}, t) &:= \nabla \cdot [p(\mathbf{x}, t)\nabla V(\mathbf{x}, t)] + \nabla \cdot [\nabla \cdot (p(\mathbf{x}, t)\mathbf{D}(\mathbf{x}, t))] \quad \forall (\mathbf{x}, t) \in \mathbb{R}^d \times \mathbb{R}^+ \\ \int_{\mathbb{R}^d} p(\mathbf{x}, t)d\mathbf{x} &= 1, \quad p(\mathbf{x}, t) \geq 0 \quad \forall (\mathbf{x}, t) \in \mathbb{R}^d \times \mathbb{R}^+ \end{aligned} \quad (2)$$

where $\mathbf{x} \in \mathbb{R}^d$ denotes a random vector, $V(\mathbf{x}, t)$ is a potential function, $\mathbf{D}(\mathbf{x}, t)$ is a diffusion matrix, $p(\mathbf{x}, t)$ is the unknown probability density function of \mathbf{x} , and \mathcal{L} denotes the partial differential operator. Following [1], the potential function $V(\mathbf{x}, t)$ and the diffusion matrix $\mathbf{D}(\mathbf{x}, t)$ can be expressed as

$$\begin{aligned} \nabla V(\mathbf{x}, t) &= -\boldsymbol{\mu}(\mathbf{x}, t), \\ \mathbf{D}(\mathbf{x}, t) &= \frac{1}{2}\mathbf{G}(\mathbf{x}, t)\mathbf{G}(\mathbf{x}, t)^\top. \end{aligned}$$

In this work, we focus on the stationary solution of (2), i.e., the invariant measure independent of time,

$$\mathcal{L}p(\mathbf{x}) = \nabla \cdot [p(\mathbf{x})\nabla V(\mathbf{x})] + \nabla \cdot [\nabla \cdot (p(\mathbf{x})\mathbf{D}(\mathbf{x}))] = 0, \quad (3)$$

with the boundary condition

$$p(\mathbf{x}) \rightarrow 0 \quad \text{as} \quad \|\mathbf{x}\|_2 \rightarrow \infty, \quad (4)$$

and some extra constraints on $p(\mathbf{x})$

$$\int_{\mathbb{R}^d} p(\mathbf{x})d\mathbf{x} = 1, \quad \text{and} \quad p(\mathbf{x}) \geq 0, \quad (5)$$

where $\|\mathbf{x}\|_2$ indicates the ℓ_2 norm of \mathbf{x} .

There are several difficulties for the approximation of equation (3). First, the boundary condition and the constraints of $p(\mathbf{x})$ may not be easily satisfied when we employ the traditional approaches such as the finite element method. Since the support of $p(\mathbf{x})$ is \mathbb{R}^d , the computation domain has to be truncated, implying that the boundary

condition must be approximated, e.g., a homogeneous boundary condition. To preserve the nonnegativity of $p(\mathbf{x})$, a projection step is needed for the box constraint. Second, it requires a fine mesh to capture the whole information when the target density is multimodal, i.e., the potential function $V(\mathbf{x})$ has many local minima [43], which is computationally infeasible when the dimension d is even moderately large. We also note that a homogeneous boundary condition usually requires a large computational domain, which makes a uniform refinement even more challenging, if no prior information can be used for certain adaptivity on mesh generation. To address these issues, we will propose an adaptive deep density approximation method to solve the Fokker-Planck equation (3) using a deep generative model for $p(\mathbf{x})$. The flow-based generative model not only provides an explicit density function that satisfies naturally all constraints on $p(\mathbf{x})$, but also suggests a simple but effective adaptive strategy for the approximation of equation (3) through sampling the current approximation of $p(\mathbf{x})$.

3. Flow-based generative model via a new affine coupling layer

In this section, we review the flow-based generative model for density estimation following the presentation in [35], and discuss our novel effective affine coupling layers which have been outlined in our recently published letter [44]. These affine coupling layers are essential for efficient flow-based generative modeling. Let $X \in \mathbb{R}^d$ be a random vector associated with a given data set, and its probability density function (PDF) is denoted by $p(\mathbf{x})$. Our target is to estimate the PDF of X using available data points. Let $Z \in \mathbb{R}^d$ be a random vector associated with a probability density function $p(z)$, where $p(z)$ is a prior distribution (e.g., Gaussian distributions). The flow-based generative modeling is to seek an invertible mapping $Z = f(X)$ where $f(\cdot)$ is a bijection: $f : X \mapsto Z$. By the change of variables formula, the following equation holds

$$p_X(\mathbf{x}) = p_Z(f(\mathbf{x})) |\det \nabla_{\mathbf{x}} f|. \quad (6)$$

Once the prior distribution $p_Z(z)$ is specified, equation (6) provides an explicit probability density function of \mathbf{x} . In flow-based generative models, an invertible mapping $f(\cdot)$ is constructed by stacking a sequence of simple bijections, each of which is a shallow neural network, and thus the overall mapping is a deep neural network. This way, a highly nonlinear PDF function can be represented, although the prior distribution for Z is simple. The mapping $f(\cdot)$ can be written in a composite form:

$$z = f(\mathbf{x}) = f_{[L]} \circ \dots \circ f_{[1]}(\mathbf{x}), \quad (7)$$

where $f_{[i]}$ is called an affine coupling layer at stage i . Given a set of training data, the invertible mapping $f(\cdot)$ can be learned by maximizing the likelihood or minimizing the cross entropy, which also provides a convenient way to sample X as $X = f^{-1}(Z)$ thanks to the invertibility of $f(\cdot)$.

3.1. A new affine coupling layer

The inverse of f is

$$\mathbf{x} = f^{-1}(z) = f_{[1]}^{-1} \circ \dots \circ f_{[L]}^{-1}(z), \quad (8)$$

and the Jacobian can be obtained by the chain rule of differentiation

$$|\det \nabla_{\mathbf{x}} f| = \prod_{i=1}^L |\det \nabla_{\mathbf{x}_{[i-1]}} f_{[i]}|, \quad (9)$$

where $\mathbf{x}_{[i-1]}$ indicate the intermediate variables with $\mathbf{x}_{[0]} = \mathbf{x}$ and $\mathbf{x}_{[L]} = \mathbf{z}$. Equations (8) and (9) suggest that the inverse and the Jacobian of $f_{[i]}(\cdot)$ should be computed efficiently. Let $\mathbf{x}_{[i]} = [\mathbf{x}_{[i],1}, \mathbf{x}_{[i],2}]^\top$ be a partition of $\mathbf{x}_{[i]}$ with $\mathbf{x}_{[i],1} \in \mathbb{R}^m$ and $\mathbf{x}_{[i],2} \in \mathbb{R}^{d-m}$ for $i = 0, \dots, L-1$. We propose a new affine coupling layer $f_{[i]}$ as follows

$$\begin{aligned} \mathbf{x}_{[i],1} &= \mathbf{x}_{[i-1],1} \\ \mathbf{x}_{[i],2} &= \mathbf{x}_{[i-1],2} \odot (1 + \alpha \tanh(s_i(\mathbf{x}_{[i-1],1}))) + e^{\beta_i} \odot \tanh(t_i(\mathbf{x}_{[i-1],1})), \end{aligned} \quad (10)$$

where $s_i : \mathbb{R}^m \mapsto \mathbb{R}^{d-m}$ and $t_i : \mathbb{R}^m \mapsto \mathbb{R}^{d-m}$ are the scaling and the translation depending on $\mathbf{x}_{[i-1],1}$, and \odot is the Hadamard product or element-wise product. The parameters $\beta_i \in \mathbb{R}^{d-m}$ are trainable variables and α is a hyper parameter. The inverse of $f_{[i]}$ is straightforward:

$$\begin{aligned} \mathbf{x}_{[i-1],1} &= \mathbf{x}_{[i],1} \\ \mathbf{x}_{[i-1],2} &= \left(\mathbf{x}_{[i],2} - e^{\beta_i} \odot \tanh(t_i(\mathbf{x}_{[i-1],1})) \right) \odot (1 + \alpha \tanh(s_i(\mathbf{x}_{[i-1],1})))^{-1}. \end{aligned} \quad (11)$$

The Jacobian of $f_{[i]}$ is

$$\nabla_{\mathbf{x}_{[i-1]}} f_{[i]} = \begin{bmatrix} \mathbf{I} & \mathbf{0} \\ \nabla_{\mathbf{x}_{[i-1],1}} \mathbf{x}_{[i],2} & \text{diag}(1 + \alpha \tanh(s_i(\mathbf{x}_{[i-1],1}))) \end{bmatrix}, \quad (12)$$

whose determinant can be efficiently computed due to the lower triangular structure. It can be seen that computing $|\nabla_{\mathbf{x}_{[i-1]}} f_{[i]}|$ does not involve the gradients of $s_{[i]}$ and $t_{[i]}$, which implies that the mappings $s_{[i]}$ and $t_{[i]}$ can be arbitrarily complicated. We model them using a neural network $\text{NN}_{[i]}$

$$(s_i, t_i) = \text{NN}_{[i]}(\mathbf{x}_{[i-1],1}). \quad (13)$$

Compared to the original affine coupling layer given in [35]

$$\begin{aligned} \mathbf{x}_{[i],1} &= \mathbf{x}_{[i-1],1} \\ \mathbf{x}_{[i],2} &= \mathbf{x}_{[i-1],2} \odot \exp(\log s_i(\mathbf{x}_{[i-1],1})) + t_i(\mathbf{x}_{[i-1],1}), \end{aligned} \quad (14)$$

our affine coupling layer has the following advantages. First, the first term of the second equation in (10) adapts the trick of ResNet [45], where an identity mapping is added to ease the training process. Second, the constant $\alpha \in (0, 1)$ is introduced to improve numerical stability. It can be seen from (12), the range of $\nabla_{\mathbf{x}_{[i-1]}} f_{[i]}$ is $[(1 - \alpha)^{d-m}, (1 + \alpha)^{d-m}]$, while the range of the gradient of coupling layers in the original real NVP is $(0, +\infty)$ [35]. Our formulation can alleviate the illnesses when the determinant of the Jacobian in the original real NVP occasionally becomes too large or too small. The another difference here is to introduce a trainable factor e^{β_i} for each affine coupling layer. Compared with $t_i(\mathbf{x}_{[i-1],1})$, e^{β_i} depends on the data points directly instead of the value of $\mathbf{x}_{[i-1]}$, which helps to reduce the number of outliers for generating samples [44].

Since the affine coupling layer $f_{[i]}$ only updates a part of $\mathbf{x}_{[i-1]}$, a series of affine coupling layers need to be stacked together to form an entire update. For example, the components $\mathbf{x}_{[i-1],1}$ that are left unchanged in the affine coupling

layer $f_{[i]}$ are updated in the next $f_{[i+1]}$, i.e., for affine coupling layer $f_{[i+1]}$, the update procedure is

$$\begin{aligned}\mathbf{x}_{[i+1],1} &= \mathbf{x}_{[i],1} \odot (1 + \alpha \tanh(s_{i+1}(\mathbf{x}_{[i],2}))) + e^{\beta_{i+1}} \odot \tanh(t_{i+1}(\mathbf{x}_{[i],2})) \\ \mathbf{x}_{[i+1],2} &= \mathbf{x}_{[i],2},\end{aligned}$$

where $s_{i+1} : \mathbb{R}^{d-m} \mapsto \mathbb{R}^m$ and $t_{i+1} : \mathbb{R}^{d-m} \mapsto \mathbb{R}^m$ are the scaling and the translation depending on $\mathbf{x}_{[i],2}$.

3.2. Scale and bias layer

It is known that batch normalization can improve training performance and stability of deep neural networks. The main idea of batch normalization is that normalizing the input of each layer by centering and scaling, which can mitigate internal covariate shift [46]. Let $\tilde{\mu}_{[i]}$ and $\tilde{\sigma}_{[i]}^2$ denote the mean and the variance of the input in layer $f_{[i]}$ estimated from the mini-batch. The batch normalization is implemented as follows. For each $\mathbf{x}_{[i]}, i = 1, \dots, L-1$, the normalization is first computed through

$$\mathbf{x}_{[i]} \leftarrow \frac{\mathbf{x}_{[i]} - \tilde{\mu}_{[i]}}{\sqrt{\tilde{\sigma}_{[i]}^2 + \epsilon}}, \quad i = 1, \dots, L-1, \quad (15)$$

where ϵ is a small constant (e.g., 10^{-6}) added in the denominator for numerical stability. After that, a transformation step to restore the representation of $f_{[i]}$ (for $i = 1, \dots, L-1$) is defined as

$$\hat{\mathbf{x}}_{[i]} = \gamma_{[i]} \mathbf{x}_{[i]} + \beta_{[i]}, \quad (16)$$

where $\gamma_{[i]}$ and $\beta_{[i]}$ are trainable variables. When the size of the mini-batch is small, the batch normalization (15) becomes less effective due to the noise involved in computing $\tilde{\mu}_{[i]}$ and $\tilde{\sigma}_{[i]}^2$. Following [36], a simplified version of the batch normalization for flow-based generative models is defined as

$$\hat{\mathbf{x}}_{[i]} = \mathbf{a}_i \odot \mathbf{x}_{[i]} + \mathbf{b}_i, \quad i = 1, \dots, L, \quad (17)$$

where \mathbf{a}_i and \mathbf{b}_i are trainable variables corresponding to the affine coupling layer $f_{[i]}$, and $\mathbf{x}_{[i]}$ are the output of $f_{[i-1]}$. The parameters \mathbf{a}_i and \mathbf{b}_i are initialized by the statistic mean and variance associated with the batch data. However, \mathbf{a}_i and \mathbf{b}_i are treated as trainable parameters that are independent of the data after initialization. This procedure is called the scale and bias layer, which is a variant of the batch normalization. Our experiments show that the scale and bias layer is simple but effective, which provides a comparable performance to the batch normalization layer in our problem setting.

4. KRnet

As discussed in section 3, the flow-based generative model relies on a sequence of bijections $f_{[i]}$ (for $i = 1, \dots, L$), each of which updates a part of $\mathbf{x}_{[i]}$. With these bijections, the input vector \mathbf{x} becomes fully correlated after two affine coupling layers. Indeed, it can be seen from (10) that the modification of $\mathbf{x}_{[i],2}$ depends on $\mathbf{x}_{[i],1}$. At the next bijection, $\mathbf{x}_{[i+1],1}$ is updated, which depends on not only $\mathbf{x}_{[i],2}$ but also $\mathbf{x}_{[i],1}$ through the modification $\mathbf{x}_{[i],2}$ in the previous bijection.

There are some concerns about such a strategy: 1) How should we partition the vector? Can we provide a mechanism to let the algorithm make a more effective partition? 2) How can we increase the model capability except for increasing the depth L ? 3) Although $\mathbf{x}_{[i+2]}$ depends on $\mathbf{x}_{[i]}$ after two consecutive affine coupling layers, the dependence is not completely nonlinear. Can we provide a nonlinear bijection at least in a component-wise way?

We have proposed a new invertible mapping called KRnet to partially address the above questions. The main idea of KRnet is to integrate the triangular structure of the Knothe-Rosenblatt rearrangement into the definition of the invertible mapping. We also propose a rotation layer for adaptive partition and a component-wise nonlinear layer. The results in this section have been outlined in a recently published letter [44]. We in this work provide more details for both the algorithm and experiments.

4.1. The overall structure of KRnet

Let μ_Z and μ_X be two Borel probability measures on \mathbb{R}^d , a mapping $\mathcal{T}: \mathbb{R}^d \mapsto \mathbb{R}^d$ is called a transport map between μ_Z and μ_X such that $\mathcal{T}_\# \mu_Z = \mu_X$, where $\mathcal{T}_\# \mu_Z$ is the push-forward of μ_Z such that $\mu_X(B) = \mu_Z(\mathcal{T}^{-1}(B))$ for every Borel set B [39]. The Knothe-Rosenblatt rearrangement tells us that the transport map \mathcal{T} has a lower-triangular structure

$$\mathbf{z} = \mathcal{T}^{-1}(\mathbf{x}) = \begin{bmatrix} \mathcal{T}_1(x_1) \\ \mathcal{T}_2(x_1, x_2) \\ \vdots \\ \mathcal{T}_N(x_1, \dots, x_N) \end{bmatrix}. \quad (18)$$

This mapping can be regarded as a limit of sequence of optimal transport maps when the quadratic cost degenerates [39]. Inspired by the Knothe-Rosenblatt rearrangement, we propose KRnet as a generalization of real NVP [35]. Let $\mathbf{x} = [\mathbf{x}^{(1)}, \dots, \mathbf{x}^{(K)}]^\top$ be a partition of \mathbf{x} , where $\mathbf{x}^{(i)} = [x_1^{(i)}, \dots, x_m^{(i)}]^\top$ with $1 \leq K \leq d$, $1 \leq m \leq d$, and $\sum_{i=1}^K \dim(\mathbf{x}^{(i)}) = d$.

Our KRnet takes an overall form

$$\mathbf{z} = f_{\text{KR}}(\mathbf{x}) = \begin{bmatrix} f_1(\mathbf{x}^{(1)}) \\ f_2(\mathbf{x}^{(1)}, \mathbf{x}^{(2)}) \\ \vdots \\ f_K(\mathbf{x}^{(1)}, \dots, \mathbf{x}^{(K)}) \end{bmatrix}, \quad (19)$$

where each f_i is an invertible mapping defined by (7) for $i = 1, \dots, K$. Note that the structure of KRnet is consistent with the Knothe-Rosenblatt rearrangement. KRnet consists of one outer loop and multiple inner loops, where the outer loop has $K - 1$ stages, corresponding to the K mappings f_i in (19), and each inner loop has L affine coupling layers. More specifically, we have

$$\mathbf{z} = f_{\text{KR}} = L_N \circ f_{[K-1]}^{\text{outer}} \circ \dots \circ f_{[1]}^{\text{outer}}(\mathbf{x}), \quad (20)$$

where $f_{[i]}^{\text{outer}}$ is defined as

$$f_{[k]}^{\text{outer}} = L_S \circ f_{[k,L]}^{\text{inner}} \circ \dots \circ f_{[k,1]}^{\text{inner}} \circ L_R \quad (21)$$

with $f_{[k,i]}^{\text{inner}}$ indicates a combination of one affine coupling layer and one scale and bias layer, and L_N , L_S and L_R indicates the nonlinear layer, the squeezing layer and the rotation layer, respectively, which will be defined later. The flow chart of KRnet can be illustrated in Figure 1.

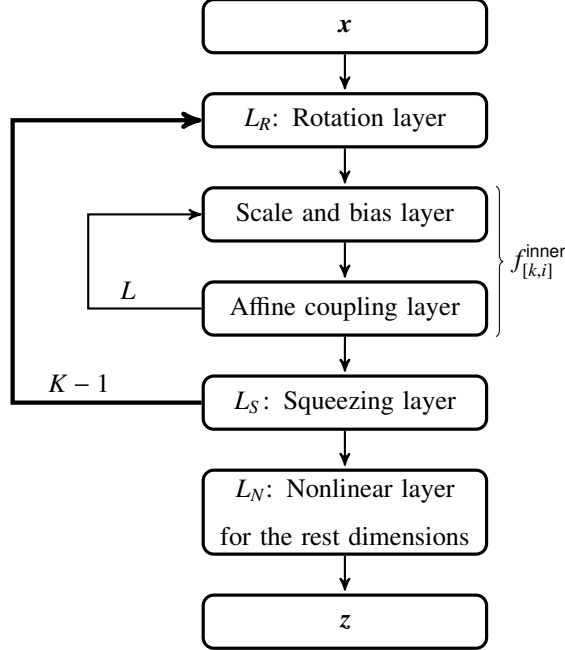


Figure 1: The flow chart of KRnet.

Let us look at how the information flows in the KRnet. Each $\mathbf{x}_{[k]} = [\mathbf{x}_{[k]}^{(1)}, \dots, \mathbf{x}_{[k]}^{(K)}]^\top$ has the same partition with $\mathbf{x}_{[k]} = f_{[k]}^{\text{outer}}(\mathbf{x}_{[k-1]})$ with $\mathbf{x}_{[0]} = \mathbf{x}$, $k = 1, \dots, K - 1$. At the beginning, a sequence of affine coupling layers in $f_{[1]}^{\text{outer}}$ is applied to the partition $\mathbf{x}_{[0]} = [\mathbf{x}_{[0]}^{(1:K-1)}, \mathbf{x}_{[0]}^{(K)}]^\top$, where $\mathbf{x}_{[0]}^{(1:K-1)}$ includes $\mathbf{x}_{[0]}^{(i)}$, $i = 1, \dots, K - 1$. From then on, the last partition $\mathbf{x}_{[k]}^{(K)}$ will remain fixed for $k > 1$. For the next iteration $f_{[2]}^{\text{outer}}$, the partition $[\mathbf{x}_{[1]}^{(1:K-2)}, \mathbf{x}_{[1]}^{(K-1)}]^\top$ will be used with $\mathbf{x}_{[1]}^{(K)}$ being deactivated. In general, after the stage $K - i + 1$ of the outer loop, the i -th partition of $\mathbf{x}_{[k]}^{(i)}$ will become deactivated, in addition to the dimensions that are deactivated in previous stages.

4.2. Squeezing layer L_S

Since each $\mathbf{x}_{[k]}$ has the same partition for $k = 1, \dots, K - 1$, we generically denote $\mathbf{x}_{[k]}$ as \mathbf{x} to simplify notation in this part. The squeezing layer is used to deactivate some dimensions using a mask

$$\mathbf{q} = [\underbrace{1, \dots, 1}_n, \underbrace{0, \dots, 0}_{d-n}]^\top. \quad (22)$$

The first n components of \mathbf{x} will be updated, while the other $d - n$ components will remain unchanged. More specifically, the partitions $\mathbf{x}^{(K-i+1)}, \dots, \mathbf{x}^{(K)}$ will remain unchanged at the $(i + 1)$ -th stage, for $i = 1, \dots, K - 1$, i.e., $n = d - \sum_{k=K-i+1}^K \dim(\mathbf{x}^{(k)})$.

4.3. Rotation layer L_R

The rotation layer defines a linear mapping of the input \mathbf{x}

$$\hat{\mathbf{x}} = \hat{\mathbf{W}}\mathbf{x},$$

through a trainable matrix

$$\hat{\mathbf{W}} = \begin{bmatrix} \mathbf{W} & \mathbf{0} \\ \mathbf{0} & \mathbf{I} \end{bmatrix} \in \mathbb{R}^{d \times d},$$

where $\mathbf{W} \in \mathbb{R}^{n \times n}$, n is defined in \mathbf{q} (see (22)), and $\mathbf{I} \in \mathbb{R}^{(d-n) \times (d-n)}$ is an identity matrix. We call it a rotation layer because we mainly expect $\hat{\mathbf{W}}$ to provide a rotation of the coordinate system. For the input of each $f_{[k]}^{\text{outer}}(\cdot)$, the coordinate system for the current active dimensions will be rotated before a partition is applied. The matrix $\hat{\mathbf{W}}$ is trainable, which provides a possibility for the algorithm to determine which dimensions should be deactivated first.

From the computation point of view, the difficulty is to compute the determinant of $\hat{\mathbf{W}}$. Instead of training $\hat{\mathbf{W}}$, we consider its LU decomposition

$$\hat{\mathbf{W}} = \begin{bmatrix} \mathbf{L} & \mathbf{0} \\ \mathbf{0} & \mathbf{I} \end{bmatrix} \begin{bmatrix} \mathbf{U} & \mathbf{0} \\ \mathbf{0} & \mathbf{I} \end{bmatrix}, \quad (23)$$

where $\mathbf{L} \in \mathbb{R}^{n \times n}$ is a unit lower triangular matrix, and $\mathbf{U} \in \mathbb{R}^{n \times n}$ is an upper triangular matrix. The determinant of $\hat{\mathbf{W}}$ is

$$\det \hat{\mathbf{W}} = \det \mathbf{L} \det \mathbf{U} = \det \mathbf{U} = \prod_{i=1}^n u_{ii}. \quad (24)$$

Entries below the main diagonal of \mathbf{L} and entries in the upper triangle of \mathbf{U} are trainable. In practice, we may simply initialize both \mathbf{L} and \mathbf{U} as an identity matrix without enforcing any constraint on $\hat{\mathbf{W}}$, although a rotation corresponds to an orthogonal matrix. Numerical experiments show that such a simplification works well. The initialization of $\hat{\mathbf{W}}$ can also be data driven. We may estimate the covariance matrix of the active dimensions with some mini-batches, and then initialize each row of $\hat{\mathbf{W}}$ using the eigenvectors of the covariance matrix. In particular, we order the eigenvectors such that from the first row of $\hat{\mathbf{W}}$ to the last one the corresponding eigenvalues decreases. This way, the least important dimensions in terms of the covariance matrix are put at the end, which will be deactivated by the next squeezing layer.

4.4. Nonlinear layer L_N

We here introduce a nonlinear layer to provide a component-wise nonlinear transformation. For simplicity, we only consider one component x of the data. We start with a nonlinear mapping $F(s) : [0, 1] \mapsto [0, 1]$:

$$F(s) = \int_0^s p(t)dt, \quad (25)$$

where $p(s)$ is a probability density function. Let $0 = s_0 < s_1 < \dots < s_{\hat{m}+1} = 1$ be a uniform mesh of the interval $[0, 1]$ with element size $h = s_{i+1} - s_i = \frac{1}{\hat{m}}$. Define $p(s)$ as a piece-wise linear polynomial

$$p(s) = \frac{w_{i+1} - w_i}{h}(s - s_i) + w_i, \quad \forall s \in [s_i, s_{i+1}], \quad (26)$$

where

$$p(s_i) = w_i.$$

Then $F(s)$, corresponding to a cumulative distribution function, is a quadratic function

$$F(s) = \frac{w_{i+1} - w_i}{2h}(s - s_i)^2 + w_i(s - s_i) + \sum_{k=0}^{i-1} \frac{w_k + w_{k+1}}{2}h, \quad \forall s \in [s_i, s_{i+1}], \quad (27)$$

whose inverse and derivative can be explicitly computed.

As the support of each dimension of \mathbf{x} is $(-\infty, \infty)$, a question is how to apply $F(s)$ to the data. A straightforward strategy is to map $(-\infty, \infty)$ to $(0, 1)$ before $F(s)$ is applied. However, when the inverse is considered, the singularity of mapping a finite interval to an infinite one may introduce issues on robustness. To allerviate this problem, we decompose $(-\infty, \infty) = (-\infty, -a) \cup [-a, a] \cup (a, \infty)$ with $a > 0$, and define the following nonlinear mapping

$$\hat{F}(x) = \begin{cases} \beta_s(x - a) + a, & x \in (-\infty, -a) \\ 2aF\left(\frac{x+a}{2a}\right) - a, & x \in [-a, a] \\ \beta_s(x + a) - a, & x \in (a, \infty), \end{cases} \quad (28)$$

where $\beta_s > 0$ is a scaling factor. It is seen that we only consider a nonlinear mapping for the data located in $[-a, a]$ and $\hat{F}(x)$ maps $[-a, a]$ to itself. On $(-\infty, -a) \cup (a, \infty)$, $\hat{F}(x)$ is simply a linear mapping. The reasoning of such a strategy is that the range of data in the training set is always finite, and after being well scaled and shifted the data will be roughly centered at the origin, implying that a nonlinear mapping on $[-a, a]$ is sufficient as long as a is large enough. To maintain the invertibility, we require some regularity at $x = \pm a$. More specifically, $\hat{F}'(x)$ should exist at $x = \pm a$. Since $\hat{F}'(x) = \beta_s$ on $(-\infty, -a) \cup (a, \infty)$, we have, on $[-a, a]$, $\hat{F}'(x)|_{x=\pm a} = F'(s)|_{s=0,1} = p(s)|_{s=0,1} = \beta_s$. So the trainable parameters include $p(s_i) = w_i$, $i = 1, \dots, \hat{m}$, subjet to the constraint $\int_0^1 p(s)ds = 1$.

Remark 1. Since the nonlinear layer is component-wise and we only apply it before the final output (see Figure 1), it provides an enlarged family of prior distributions other than the commonly used Gaussian prior. The parameter β_s acts as an estimate of the density $p(s)$ at $s = 0, 1$. If a is sufficiently large, β_s can be small accordingly. The prior distribution is often chosen as the standard Gaussian, which means that the density is larger around the origin when the data pass the nonlinear layer. This suggests we may consider an adaptive mesh for more effectiveness, in other words, the mesh is finer around $s = 1/2$ and coarser around $s = 0, 1$.

4.5. The complexity of KRnet

We count the number of trainable parameters in KRnet. For simplicity, we assume that each $f_{[k]}^{\text{outer}}$ has L general coupling layers $f_{[k,i]}^{\text{inner}}$. Let d_k be the number of effective dimensions for $f_{[k]}^{\text{outer}}$ and $N_{\text{NN},k}$ the number of model parameters for the neural network (13) used in $f_{[k,i]}^{\text{inner}}$. We note that the main characetristic of KRnet is that a portion of dimensions will be deactivated as k increases. As d_k decreases with k , we expect that the neural network (13) in $f_{[k,i]}^{\text{inner}}$ should become simpler for a larger k . In other words, $N_{\text{NN},k}$ may decrease as k increases. For simplicity, we let $N_{\text{NN},k} = rN_{\text{NN},k-1}$, where $0 < r < 1$, without worrying about the detailed configuration of the neural network. The number of trainable parameters is d_k^2 for L_R , and $\hat{m}d$ for L_N , and $2d_k$ for the scale and bias layer. Assume that $d = mK$. We have $d_k = d - (k-1)m$, $k = 1, \dots, K$. According to the flow chart in Figure 1, we have the total number of model parameters as

$$N_{\text{dof}} = \hat{m}d + \sum_{k=1}^{K-1} (N_{\text{NN},1}r^{k-1}L + (K-k+1)^2m^2 + 2(K-k+1)mL). \quad (29)$$

The model complexity is mainly determined by the depth L and the number K for the partition of data.

4.6. KRnet for density estimation

We study the performance of KRnet for density estimation in this part. The comparison between the real NVP and the KRnet is presented. Once the KRnet is constructed, we can utilize the maximum likelihood method to train our model, since the probability density function is explicit (see (6)). In our setting, an estimated density function is parameterized with Θ , and density estimation here is to optimize the parameter Θ using given training data sets. Denoting the training data set $\mathcal{S} = \{\mathbf{x}^{(i)}\}_{i=1}^{N_t}$ for $p_X(\mathbf{x})$ which is unknown, the maximum likelihood estimator for Θ is

$$\Theta^* = \arg \max_{\Theta} \prod_{i=1}^{N_t} p_X(\mathbf{x}^{(i)}; \Theta) = \arg \max_{\Theta} \frac{1}{N_t} \sum_{i=1}^{N_t} \log p_X(\mathbf{x}^{(i)}; \Theta), \quad (30)$$

where $p_X(\mathbf{x}; \Theta)$ is a probability density function defined by our KRnet parameterized with Θ . We consider minimizing the Kullback-Liebler (KL) divergence between the exact density $p_X(\mathbf{x})$ and the model $p_X(\mathbf{x}; \Theta)$

$$\min_{\Theta} D_{KL}(p_X(\mathbf{x}) \| p_X(\mathbf{x}; \Theta)) = \mathbb{E}_{\mathbf{x} \sim p_X(\mathbf{x})} \left[\log \frac{p_X(\mathbf{x})}{p_X(\mathbf{x}; \Theta)} \right] = H(p_X(\mathbf{x}), p_X(\mathbf{x}; \Theta)) - H(p_X(\mathbf{x})) \quad (31)$$

where $H(p_X(\mathbf{x}))$ is the entropy of $p_X(\mathbf{x})$ and $H(p_X(\mathbf{x}), p_X(\mathbf{x}; \Theta))$ is the cross entropy of $p_X(\mathbf{x})$ and $p_X(\mathbf{x}; \Theta)$. Since $p_X(\mathbf{x})$ is independent of Θ , minimizing the KL divergence is equivalent to minimizing the cross entropy. Note that

$$H(p_X(\mathbf{x}), p_X(\mathbf{x}; \Theta)) \approx -\frac{1}{N_t} \sum_{i=1}^{N_t} \log p_X(\mathbf{x}^{(i)}; \Theta) \quad (32)$$

implying minimizing the cross entropy is the same as maximizing the likelihood. To measure the quality of KRnet, we compute the KL divergence (31) on a validation set between a reference PDF and the trained density model.

The training data sets $\mathcal{S} = \{\mathbf{x}^{(i)}\}_{i=1}^{N_t}$ for density estimation are generated as follows. Assume that X has i.i.d. components and each component $X_i \sim \text{Logistic}(0, s)$ has a PDF $\rho(x_i; 0, s)$. We generate a sample $\mathbf{x}^{(i)}$ of X , and then check if it satisfies the following constraint:

$$\left\| \mathbf{R}_{\gamma, \theta_j} [x_j^{(i)}, x_{j+1}^{(i)}]^\top \right\|_2 \geq C, \quad j = 1, \dots, d-1, \quad (33)$$

where C is a specified constant, and

$$\mathbf{R}_{\gamma, \theta_j} = \begin{bmatrix} \gamma & 0 \\ 0 & 1 \end{bmatrix} \begin{bmatrix} \cos \theta_j & -\sin \theta_j \\ \sin \theta_j & \cos \theta_j \end{bmatrix}, \quad \theta_j = \begin{cases} \frac{\pi}{4}, & \text{if } j \text{ is even} \\ \frac{3\pi}{4}, & \text{otherwise} \end{cases}.$$

The sample $\mathbf{x}^{(i)}$ will be accepted if the constraint (33) is satisfied and rejected otherwise. This way, an elliptic hole is generated for any two adjacent dimensions of data points. The reference PDF is then defined as

$$p_X(\mathbf{x}) = \frac{I_B(\mathbf{x}) \prod_{i=1}^d \rho(x_i; 0, s)}{\mathbb{E}[I_B(X)]}, \quad (34)$$

where B is the set defined by equation (33) and $I_B(\cdot)$ is an indicator function with $I_B(\mathbf{x}) = 1$ if $\mathbf{x} \in B$; 0, otherwise. For this test problem, we set $d = 8$, $\gamma = 3$ and $C = 7.6$. This case has been studied in [44], where the rotation layers and nonlinear layers are turned off. In [44] an algebraic convergence has been observed numerically for both the real NVP and the KRnet, where the convergence rate of KRnet is about twice as large as that of the real NVP. We here only demonstrate the effectiveness of the rotation layer and the nonlinear layer.

We now compare the performance of KRnet and real NVP numerically. In KRnet, we deactivate the dimensions by one, i.e., $K = 7$. We let $N_{\text{NN},k} = 0.9N_{\text{NN},k-1}$ by adjusting the width of the neural network $\text{NN}_{[i]}$ which consists of two fully connected hidden layers of the same width. Other configurations of $\text{NN}_{[i]}$ can also be considered. One example is given in Figure 2. The neural network $\text{NN}_{[i]}$ (for $i = 0, \dots, L-1$) consists of three hidden layers and one linear layer, where the first hidden layer and the linear layer have w neurons, and the middle two layers have $w/2$ neurons. In this experiment, we combine the two middle hidden layers to one hidden layer with w neurons. We set $w = 24$ and use the rectified linear unit function (ReLU) as the activation function [47]. The depth of the real NVP will be determined by N_{dof} of the KRnet, since we split the dimensions into two halves in real NVP. The KRnet will be implemented as follows. We train KRnet with three stages and record the errors of each stage. In the first stage, we switch off both the rotation layers and the nonlinear layers and train the model for 8000 epochs; in the second stage, we switch on the rotation layers and restart the training process for another 2000 epochs; finally, we switch on both the rotation layers and the nonlinear layers and continue the training process for another 2000 epochs. For the real NVP, we simply run 8000 epochs. For each epoch, we compute the relative error

$$\delta = \frac{D_{KL}(p_X(\mathbf{x})\|p_X(\mathbf{x}; \Theta))}{H(p_X(\mathbf{x}))} \quad (35)$$

using the validation set, since the cross entropy should converge to the differential entropy of the reference PDF. We record the minimum relative error of all epoches. Furthermore, to reduce the bias of δ , we will sample 10 independent training sets and repeat the training process ten times to obtain an averaged relative error δ . The relative errors corresponding to the above three stages of training KRnet are denoted as δ_I , δ_{II} and δ_{III} . We will sample 3.2×10^5 data points for both the training set and the validation set. We employ the Adam optimizer [48] with learning rate 0.001 and batch size 80000.

The results of numerical experiments have been summarized in Table 1. First of all, both δ_{II} and δ_{III} are smaller than δ_I , indicating that the rotation layers and nonlinear layers are able to improve the model performance. Such an improvement is more noticeable for a smaller L . Second, for the specific setup of the numerical experiments, the errors δ_i , $i = I, II, III$, of the KRnet decay consistently as L increases while the errors of the real NVP do not show consistent decay. Since we compute the errors after 8000 epochs for all L , this shows that for a comparable model complexity the KRnet needs less epoches to obtain a substantial decrease in error than the real NVP. Third, as also shown in [44], the real NVP performs better than KRnet for a small L . The real NVP can be regarded as a KRnet with a half-half partition, i.e., $K = 2$ and $m = \frac{d}{2} = 4$. For a fixed complexity, the performance of KRnet depends on both K and L . In Figure 3, we compare the approximated distributions given by the real NVP with $L = 42$ and the KRnet with $L = 8$, where both the rotation layers and the nonlinear layers are switched on.

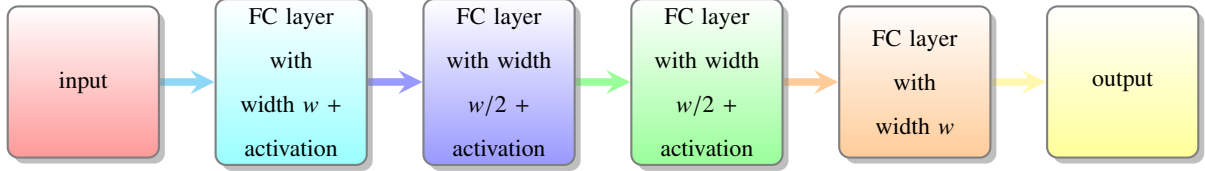


Figure 2: The architecture of $\text{NN}_{[i]}$ for affine coupling layers, for $i = 0, \dots, L - 1$ (FC layers refer to fully connected layers).

Table 1: The effects of rotation and nonlinear layers in KRnet. δ_I , δ_{II} and δ_{III} are relative errors of KRnet, respectively, for the aforementioned three stages. δ is the relative error of real NVP, whose depth is chosen to roughly match the DOFs (degrees of freedom) of the KRnets from the same column. For the nonlinear layers, we use 32 nonuniform elements to decompose $[-30, 30]$, i.e., $a = 30$. Note that the rotation layers and the nonlinear layers do not introduce a significant increase in the total number of DOFs. The percentages in parentheses indicate the degree of drop in terms of δ_I .

KRnet	$L = 2$	$L = 4$	$L = 6$	$L = 8$
δ_I	7.54e-2	2.45e-2	1.44e-2	9.50e-3
δ_{II}	6.53e-2 ($\downarrow 13\%$)	2.24e-2 ($\downarrow 9\%$)	1.39e-2 ($\downarrow 3\%$)	9.11e-3 ($\downarrow 4\%$)
δ_{III}	4.93e-2 ($\downarrow 35\%$)	1.95e-2 ($\downarrow 20\%$)	1.26e-2 ($\downarrow 13\%$)	8.34e-3 ($\downarrow 12\%$)
Real NVP	$L = 10$	$L = 20$	$L = 32$	$L = 42$
δ	2.17e-2	1.98e-2	2.11e-2	2.05e-2

5. Adaptive deep density approximation for the stationary Fokker-Planck equation

We intend to use KRnet as a PDF model to approximate the Fokker-Planck equation to alleviate the difficulties from the curse of dimensionality. In particular, we will develop an adaptive deep density approximation (ADDA) approach, which consists of two components: 1) solving the Fokker-Planck equation on a certain set of collocation points by a machine learning technique; 2) choosing a new set of collocation points to achieve a certain type of adaptivity. These two components are implemented alternately to achieve effects of adaptivity such that the efficiency will be improved.

5.1. Stochastic gradient descent based on stochastic collocation

Let $p_X(\mathbf{x}; \Theta)$ be a probability density function associated with the random vector X , which is based on the KRnet. All the constraints in (4) and (5) are naturally satisfied since $p_X(\mathbf{x}; \Theta)$ is a family of probability density functions, implying that the difficulties caused by the boundary conditions and the nonnegativity of PDF have disappeared. We seek to approximate the solution $p(\mathbf{x})$ of the Fokker-Planck equation by $p_X(\mathbf{x}; \Theta)$ to take advantage of the weaker dependence of deep neural networks on dimensionality than traditional computational approaches such as the finite element methods [49, 50, 51].

The main idea of a machine learning approach to solve PDEs is to consider an optimization problem defined on a set of collocation points where the equation is constrained. Let $p_{\text{data}}(\mathbf{x})$ be a probability density function, based on

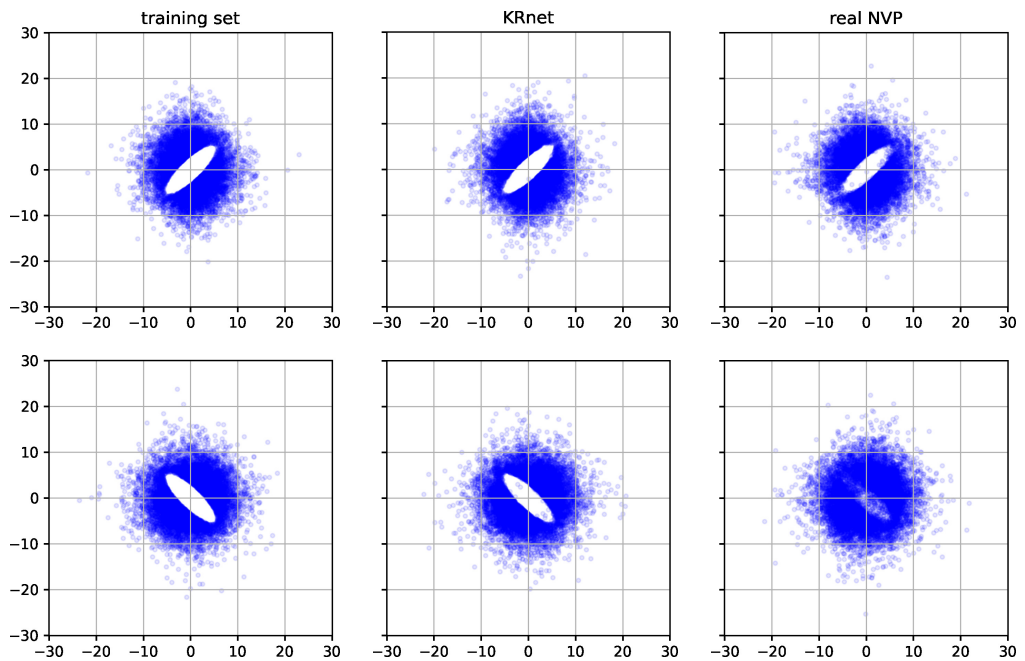


Figure 3: Training data, and data sampled from KRnet and real NVP. The first row shows the components x_1 and x_2 , and the second row shows the components x_4 and x_5 . We pick the two pairs of adjacent dimensions, which include the best and the worst performance of real NVP respectively.

which we define a loss functional

$$J(p_X(\mathbf{x}; \Theta)) = \mathbb{E}_{p_{\text{data}}(\mathbf{x})} (r^2(\mathbf{x}; \Theta)) = \mathbb{E}_{p_{\text{data}}(\mathbf{x})} (\mathcal{L}^2(p_X(\mathbf{x}; \Theta))) \quad (36)$$

where \mathbb{E} denotes the expectation, and r is the residual loss. The solution $p(\mathbf{x})$ of (3) can be approximated by $p_X(\mathbf{x}; \Theta)$ through minimizing the loss functional $J(p_X(\mathbf{x}; \Theta))$. In reality, we usually do not have much prior understanding about the residual, and simply assign $p_{\text{data}}(\mathbf{x})$ to a simple distribution, e.g., a uniform distribution defined on a finite computational domain. We then use $p_{\text{data}}(\mathbf{x})$ to sample a set $C = \{\mathbf{x}^{(i)}\}_{i=1}^N$ of collocation points to approximate the loss functional, i.e.,

$$\hat{J}(p_X(\mathbf{x}; \Theta)) = \frac{1}{N} \sum_{i=1}^N \mathcal{L}^2(p_X(\mathbf{x}^{(i)}; \Theta)) \approx J(p_X(\mathbf{x}; \Theta)), \quad (37)$$

based on which we choose the optimal parameter Θ^* :

$$\Theta^* = \arg \min_{\Theta} \hat{J}(p_X(\mathbf{x}; \Theta)). \quad (38)$$

The optimization problem (38) will be solved by the stochastic gradient descent (SGD) method [52], which is summarized as follows. The set of collocation points can be divided into n_b mini-batches $\{C_{i_b}\}_{i_b=1}^{n_b}$, where every mini-batch C_{i_b} contains m samples such that $N = mn_b$. Denoting the parameters at i_b -th iteration of a certain epoch j as $\Theta_{i_b}^{(j)}$, for every mini-batch C_{i_b} and $\mathbf{x}^{(l)} \in C_{i_b}$, $l = 1, \dots, m$, one can apply the mini-batch to estimate the expectation of the residual loss and the stochastic gradient, and then update the parameters Θ based on the following scheme

$$\Theta_{i_b}^{(j)} = \Theta_{i_b-1}^{(j)} - \eta \nabla_{\Theta} \left[\frac{1}{m} \sum_{l=1}^m (r(\mathbf{x}^{(l)}; \Theta_{i_b-1}^{(j)}))^2 \right] \quad \text{for } i_b = 1, \dots, n_b, j = 1, 2, \dots \quad (39)$$

where η is a given learning rate. Compared with the gradient descent method, the stochastic gradient descent method only requires computing the gradient on the mini-batch C_{i_b} . In practice, the Adam optimizer, which is a variant version of SGD is used to accelerate the training procedure for deep neural networks [48]. For training deep neural networks, there is no guarantee that the gradient-based algorithm could converge to the global optimum since the loss functional $\mathbb{E}_{p_{\text{data}}(\mathbf{x})} (r^2(\mathbf{x}; \Theta))$ is highly non-convex with respect to the parameters Θ [52].

5.2. Adaptive sampling procedure

Compared with the standard finite element methods (FEM) [5], the deep learning approach does not require mesh generation to solve PDEs, which shares more similarities to meshless methods, and the approximation of (36) fits naturally with SGD. Figure 4 shows a linear finite element mesh in $[0, 1]^2$ and the collocation points that are generated with a uniform distribution in $[0, 1]^2$.

Adaptivity plays an important role in classical numerical methods for the approximation of PDEs. Considering a finite element method subject to a certain mesh of the computation domain, we expect that the element-wise approximation errors are distributed in a nearly uniform way. This means that the most effective mesh should be non-uniform since the regularity of the solution varies in the computation domain. In our problem, the distribution $p_{\text{data}}(\mathbf{x})$ of the collocation points will affect the approximation of $J(p_X(\mathbf{x}; \Theta))$ and the optimal parameter Θ^* as well. Apparently a uniform distribution is not an optimal choice for $p_{\text{data}}(\mathbf{x})$ especially for high-dimensional problems. For a certain

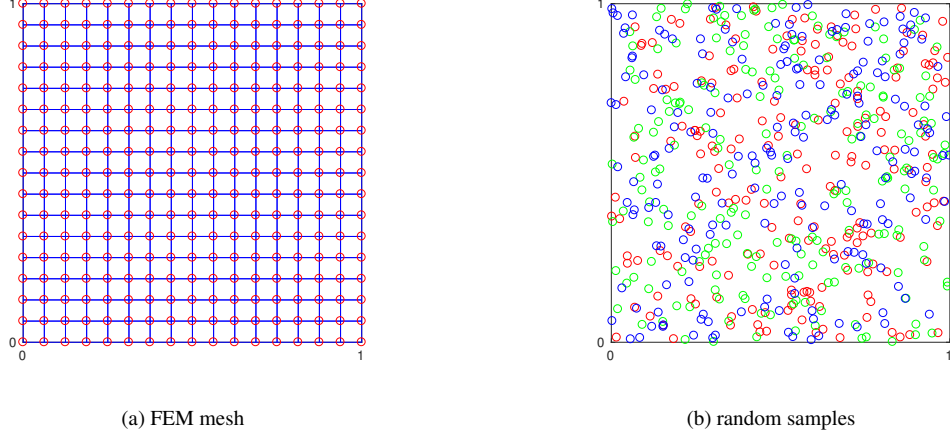


Figure 4: An example of linear finite element meshes and stochastic collocation points in $[0, 1]^2$.

amount of collocation points, the curse of dimensionality will weaken the contribution of each collocation point to our learning problem, which will be worsen for the approximation of PDF if the exact solution $p(\mathbf{x})$ is far away from being uniform. We then expect to use samples from a nonuniform distribution $p_{\text{data}}(\mathbf{x})$ for the approximation $J(p_X(\mathbf{x}; \Theta))$, where a simple criterion is that $p_{\text{data}}(\mathbf{x})$ should be consistent with the true solution $p(\mathbf{x})$ to some extent. This will result in adaptive deep density approximation (ADDA) for the approximation of the Fokker-Planck equation.

It is, in general, difficult to generate samples that are adaptive to the true solution $p(\mathbf{x})$. Fortunately, flow-based deep generative models provide an opportunity for us to do this thanks to the invertible mapping. Our strategy is as follows. Starting with an initial set of collocation points $C_0 = \{\mathbf{x}_{(0)}^{(i)}\}_{i=1}^N$ drawn from a uniform distribution, we train and obtain the KRnet $Z = f_{\text{KR},(0)}(X; \Theta^{*,(0)})$, which corresponds to the PDF $p_X^{(0)}(\mathbf{x}; \Theta^{*,(0)})$. We then generate a new set $C_1 = \{\mathbf{x}_{(1)}^{(i)}\}_{i=1}^N$ of collocation points by $X = f_{\text{KR},(0)}^{-1}(Z)$ using N samples from the prior distribution of Z . Then C_1 is a set of samples from $p_X^{(0)}(\mathbf{x}; \Theta^{*,(0)})$. We continue to update the KRnet using $\Theta^{*,(0)}$ as the initial parameters and C_1 as the training set, which yields $f_{\text{KR},(1)}(X; \Theta^{*,(1)})$. Then another iteration starts. In general, we sample the current optimal PDF model $p_X^{(k)}(\mathbf{x}; \Theta^{*,(k)})$ to generate a new training set $C_{k+1} = \{\mathbf{x}_{(k+1)}^{(i)}\}_{i=1}^N$ and update the KRnet to $f_{\text{KR},(k+1)}(\mathbf{x}; \Theta^{*,(k+1)})$. This way, the samples for the training process becomes more and more consistent with the true solution, if $p_X^{(k)}(\mathbf{x}; \Theta^{*,(k)})$ approaches $p(\mathbf{x})$ as k increases. In other words, more collocation points will be chosen in the region of higher density while less collocation points in the region of lower density. Our adaptive training process has been summarized in Algorithm 1, where $N_{\text{adaptive}} \in \mathbb{N}$ is a given number of maximum adaptivity iterations, and this strategy is called the adaptive deep density approximation based on KRnet (ADDA-KR) in the following. The KRnet at the last step is called the ADDA-KR solution for the steady state Fokker-Planck problem (3)–(4).

We note that the adaptivity in Algorithm 1 can be further tuned. One possible strategy is to update the training set gradually for each training stage, e.g., up to a certain percentage. In this work, we replace the whole training set from the previous stage just for simplicity.

5.3. Implementation issues

When minimizing the loss functional (37), numerical underflow issues can be encountered, especially when \mathbf{x} is relatively high-dimensional. That is, the loss functional can be too small to provide an effective gradient descent direction. To alleviate this issue, we develop the following scaling strategy in our implementation. Multiplying both sides of equation (3) by a constant $C_s > 0$ gives

$$\mathcal{L}(C_s p(\mathbf{x})) = \nabla \cdot [C_s p(\mathbf{x}) \nabla V(\mathbf{x})] + \nabla \cdot [\nabla \cdot (C_s p(\mathbf{x}) \mathbf{D}(\mathbf{x}))] = 0. \quad (40)$$

The solution of the above equation is the same as the solution of the original stationary Fokker-Planck equation (3). However, if C_s is large enough, (40) is numerically more stable than (3), and the loss functional (37) associated with (40) can typically provide effective gradient descent directions to optimize the parameters Θ . In our practical implementation, we usually set $C_s = 100$.

6. Numerical study

In this section, numerical experiments are conducted to illustrate the effectiveness of our ADDA-KR (adaptive deep density approximation based on KRnet) approach presented in Algorithm 1. Five test problems for the Fokker-Planck equation are studied—one one-dimensional test problem, two two-dimensional test problems (one is a single modal distribution, and the other is a bimodal distribution), one four-dimensional test problem, and one eight-dimensional test problem. The activation function of $\text{NN}_{[i]}$ (see (13)) is set to the hyperbolic tangent function for all test problems. For comparison, we also test the performance of a direct adaptive version of classic real NVP, and as the real NVP utilizes a half-half partition (see section 4.6), we refer to it as ADDA-HH. The implementation of ADDA-HH is to replace the KRnet in ADDA-KR (Algorithm 1) by the classical real NVP, and we set the same input parameters for both ADDA-KR and ADDA-HH in all our test problems. In addition, results of non-adaptive versions of KRnet and real NVP are included for high-dimensional test problems (the four-dimensional and the eight-dimensional test problems), which are referred to as Uniform-KR and Uniform-HH. In Uniform-KR and Uniform-HH, collocation points are generated through uniform distributions, and other settings of KRnet and real NVP are the same as the settings for ADDA-KR in these test problems.

6.1. A one-dimensional test problem

We start with this one-dimensional case, where the governing equation is

$$\begin{aligned} \frac{\partial(xp(x))}{\partial x} + \frac{\sigma^2}{2} \frac{\partial^2(p(x))}{\partial x^2} &= 0 \\ \int_{\mathbb{R}} p(x) dx &= 1, \quad p(x) \geq 0 \end{aligned} \quad (41)$$

and the exact solution is

$$p(x) = \frac{\exp(-x^2)}{\sqrt{\pi}}. \quad (42)$$

For this one-dimensional problem, KRnet is the same as the classical real NVP, and the layers except affine coupling layers do not exist. As the affine coupling layers (see section 3.1) need at least two-dimensions, we use $[x, x]$ as an

Algorithm 1 Adaptive deep density approximation based on KRnet (ADDA-KR) for the Fokker-Planck equation

Input: Initial KRnet $p_X^{(0)}(\mathbf{x}; \Theta_0^{(0)})$, maximum epoch number N_e , maximum iteration number N_{adaptive} , learning rate η , batch size m , and initial training set $C_0 = \{\mathbf{x}_{(0)}^{(i)}\}_{i=1}^N$.

1: Divide $C_0 = \{\mathbf{x}_{(0)}^{(i)}\}_{i=1}^N$ into n_b mini-batch $\{C_{i_b}\}_{i_b=1}^{n_b}$.

2: **for** $k = 1 : N_{\text{adaptive}}$ **do**

3: **for** $j = 0 : N_e - 1$ **do**

4: **for** $i_b = 1 : n_b$ **do**

5: Compute the values of the residual loss $r(\mathbf{x}_{(k-1)}^{(l)}; \Theta_{i_b-1}^{(j)})$ (see (37)) for $l = 1, \dots, m$, on the mini-batch C_{i_b} .

6: Update the parameters $\Theta_{i_b}^{(j)} = \Theta_{i_b-1}^{(j)} - \eta \nabla_{\Theta} \left[\frac{1}{m} \sum_{l=1}^m (r(\mathbf{x}_{(k-1)}^{(l)}; \Theta_{i_b-1}^{(j)}))^2 \right]$.

7: **end for**

8: **if** $j = N_e - 1$ **then**

9: Let $\Theta^{*,(k)} := \Theta_{n_b}^{(N_e-1)}$.

10: **else**

11: Let $\Theta_0^{(j+1)} := \Theta_{n_b}^{(j)}$.

12: **end if**

13: Shuffle the set of collocation points $C_{k-1} = \{\mathbf{x}_{(k-1)}^{(i)}\}_{i=1}^N$.

14: Divide $C_{k-1} = \{\mathbf{x}_{(k-1)}^{(i)}\}_{i=1}^N$ into n_b mini-batch $\{C_{i_b}\}_{i_b=1}^{n_b}$.

15: **end for**

16: **if** $k = N_{\text{adaptive}}$ **then**

17: Let $\Theta := \Theta^{*,(k)}$.

18: **else**

19: Generate $C_{k+1} = \{\mathbf{x}_{(k+1)}^{(i)}\}_{i=1}^N$ by $p_X^{(k)}(\mathbf{x}; \Theta^{*,(k)})$.

20: Let $\Theta_0^{(0)} := \Theta^{*,(k)}$.

21: **end if**

22: **end for**

23: Obtain the ADDA-KR solution $p_X(\mathbf{x}; \Theta) := p_X^{(N_{\text{adaptive}})}(\mathbf{x}; \Theta)$.

Output: The ADDA-KR solution $p_X(\mathbf{x}; \Theta)$.

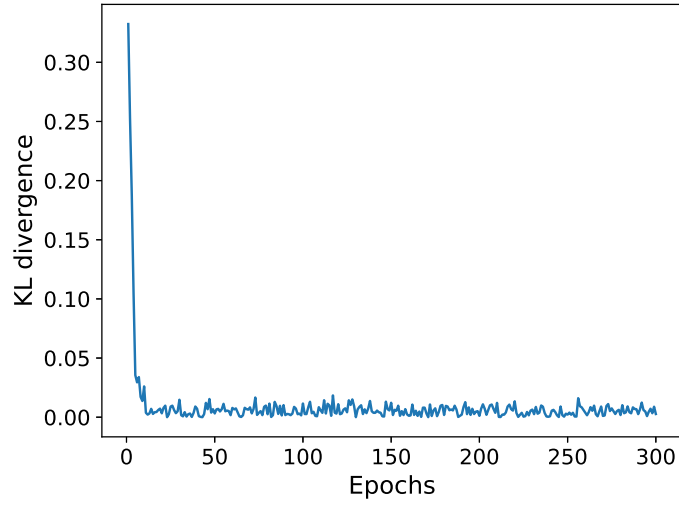


Figure 5: The KL divergence with respect to epochs, one-dimensional test problem.

input in our implementation of KRnet. We generate the initial parameters $\Theta_0^{(0)}$ for the inputs of Algorithm 1, using Glorot Gaussian initialization [53], and then construct the initial KRnet $p_X^{(0)}(x; \Theta_0^{(0)})$. The number of epochs is set to $N_e = 300$, and only one adaptivity iteration is conducted for this one-dimensional problem, i.e., $N_{\text{adaptive}} = 1$. The learning rate for Adam optimizer is set to $\eta = 0.0002$, and the batch size is set to $m = 500$. The initial training set C_0 is generated through the uniform distribution with range $[-5, 5]$, and the sample size is set to $|C_k| = 3000$ for each iteration step k for $k = 0, \dots, N_{\text{adaptive}}$. In addition, we take $L = 8$ affine coupling layers, and two fully connected layers with $w = 48$ neurons for $\text{NN}_{[i]}$ (see (13)).

To assess the accuracy of our ADDA-KR approach (Algorithm 1), we compute the KL divergence between the exact solution $p(x)$ and our ADDA-KR solution $p_X(x; \Theta)$:

$$\begin{aligned} D_{KL}(p(x) \parallel p_X(x; \Theta)) &= \int_{-\infty}^{\infty} p(x) \log p(x) dx - \int_{-\infty}^{\infty} p(x) \log p_X(x; \Theta) dx \\ &= -\frac{1}{2}(1 + \log \pi) - \int_{-\infty}^{\infty} p(x) \log p_X(x; \Theta) dx \end{aligned}$$

where the last term of the above equation is approximated by Monte Carlo integration with 10^4 samples. Figure 5 shows the KL divergence decreases to zero quickly. Figure 6 shows the exact solution $p(x)$ and our ADDA-KR solution $p_X(x; \Theta)$, where it can be seen that they are visually indistinguishable.

6.2. Two-dimensional test problems

In this part, two-dimensional Fokker-Planck equations are considered, where the solution of the first one is a single modal distribution and the solution of the second one is a bimodal distribution.

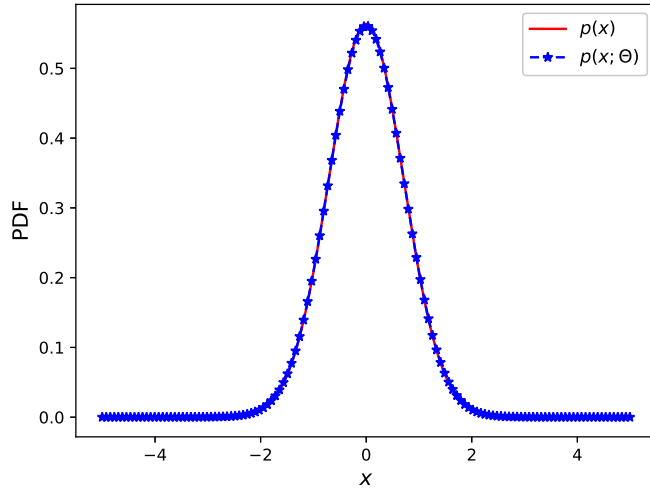


Figure 6: The exact solution and the ADDA-KR solution, one-dimensional test problem.

6.2.1. Two-dimensional single modal distribution

The stationary Fokker-Planck equation for this test problem is

$$\begin{aligned} \nabla \cdot [p(\mathbf{x}) \mathbf{A} \mathbf{x}] + \nabla \cdot [\nabla \cdot (p(\mathbf{x}) \mathbf{D})] &= 0 \\ \int_{\mathbb{R}^d} p(\mathbf{x}) d\mathbf{x} &= 1, \quad p(\mathbf{x}) \geq 0 \end{aligned} \tag{43}$$

where \mathbf{A} and \mathbf{D} are two constant matrices. This equation is corresponding to the following Ornstein-Uhlenbeck process

$$dX_t = -\mathbf{A}X_t dt + \mathbf{G}dw_t, \tag{44}$$

where $\mathbf{D} = \mathbf{G}\mathbf{G}^\top/2$.

The solution of (43) exists if the real parts of the eigenvalues of \mathbf{A} are larger than zero [1], and it can be written as

$$p(\mathbf{x}) = (2\pi)^{-1} (\det \Sigma)^{-\frac{1}{2}} \exp\left(-\frac{1}{2} \mathbf{x}^\top \Sigma^{-1} \mathbf{x}\right), \tag{45}$$

where the covariance matrix Σ is determined by the following Lyapunov equation

$$\mathbf{A}\Sigma + \Sigma\mathbf{A}^\top = 2\mathbf{D}. \tag{46}$$

The above Lyapunov equation has a unique solution if and only if the eigenvalues λ_i of \mathbf{A} satisfy $\lambda_i \neq -\lambda_j$ for all $i, j = 1, 2$. In this test problem, the constant matrix \mathbf{A} for the drift term and the diffusion matrix \mathbf{D} are set to

$$\begin{aligned} \mathbf{A} &= \begin{bmatrix} 1.37096037 & -0.48306187 \\ -0.48306187 & 1.62903963 \end{bmatrix}, \\ \mathbf{D} &= \begin{bmatrix} 22.52429192 & -6.55821381 \\ -6.55821381 & 12.68972 \end{bmatrix}, \end{aligned}$$

which implies that the covariance matrix Σ is

$$\Sigma = \begin{bmatrix} 8.12186142 & -0.26372569 \\ -0.26372569 & 3.81664391 \end{bmatrix}.$$

We generate the initial parameters $\Theta_0^{(0)}$ with Glorot Gaussian initialization [53], and then construct the initial KRnet $p_X^{(0)}(\mathbf{x}; \Theta_0^{(0)})$ for Algorithm 1. The number of epochs is set to $N_e = 300$, and two adaptivity iterations are conducted for this problem, i.e., $N_{\text{adaptive}} = 2$. The learning rate for Adam optimizer is set to $\eta = 0.0002$, and the batch size is set to $m = 1000$. The initial training set C_0 is generated through the uniform distribution with range $[-6, 6]^2$, and the sample size is set to $|C_k| = 6 \times 10^4$ for each iteration step k for $k = 0, \dots, N_{\text{adaptive}}$. In addition, we take $L = 8$ affine coupling layers, and two fully connected layers with $w = 48$ neurons for $\text{NN}_{[i]}$ (see (13)).

Figure 7 shows the exact solution $p(\mathbf{x})$ and our ADDA-KR solution $p_X(\mathbf{x}; \Theta)$, where it can be seen that they are visually indistinguishable. For this test problem, there is no significant difference between the ADDA-KR solution and the ADDA-HH solution, and we then only show the exact solution and our ADDA-KR solution. Figure 8 shows samples drawn from the exact solution of (43) and our ADDA-KR solution, which confirms that the corresponding distributions ($p(\mathbf{x})$ and $p_X(\mathbf{x}; \Theta)$) are very close.

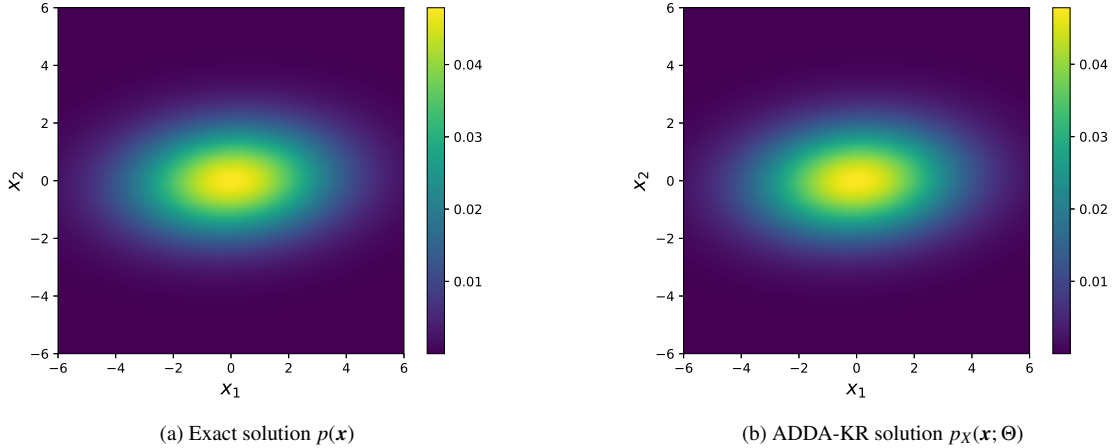


Figure 7: Solutions, two-dimensional single modal test problem.

6.2.2. Two-dimensional bimodal distribution

In this test problem, the Fokker-Planck equation considered is

$$\begin{aligned} \nabla \cdot [p(\mathbf{x}) \nabla \log(\beta_1 p_1(\mathbf{x}) + \beta_2 p_2(\mathbf{x}))] + \nabla^2 p(\mathbf{x}) &= 0 \\ \int_{\mathbb{R}^d} p(\mathbf{x}) d\mathbf{x} &= 1, \quad p(\mathbf{x}) \geq 0 \end{aligned} \tag{47}$$

where for $k = 1, 2$, each $p_k(\mathbf{x})$ is the probability density function of the normal distribution with mean μ_k and covariance Σ_k , and $\beta_1 + \beta_2 = 1$. The solution of (47) is the following Gaussian mixture distribution [43, p. 123],

$$p(\mathbf{x}) = \beta_1 p_1(\mathbf{x}) + \beta_2 p_2(\mathbf{x}). \tag{48}$$

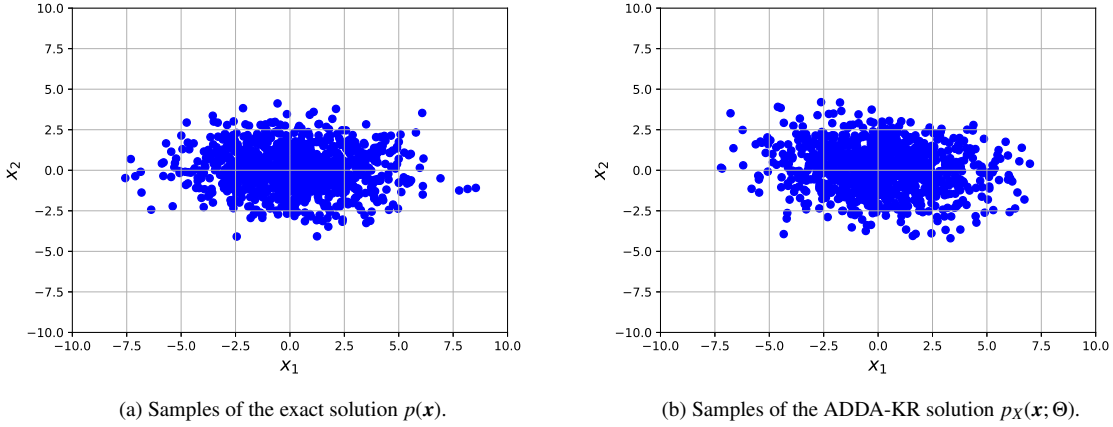


Figure 8: Samples, two-dimensional single modal test problem.

Here, we set μ_k , Σ_k and β_k for $k = 1, 2$ as

$$\begin{aligned} \beta_1 &= 0.55, \beta_2 = 0.45, \quad \mu_1 = [-1, -1]^\top, \mu_2 = [2, 2]^\top \\ \Sigma_1 &= \begin{bmatrix} 6.12186142 & -0.26372569 \\ -0.26372569 & 1.81664391 \end{bmatrix}, \quad \Sigma_2 = \begin{bmatrix} 2.8828528 & -0.70234742 \\ -0.70234742 & 2.69199911 \end{bmatrix}. \end{aligned} \quad (49)$$

The matrices Σ_1 and Σ_2 are positive definite, and their entries are randomly constructed.

We again generate the initial parameters $\Theta_0^{(0)}$ with Glorot Gaussian initialization, and then construct the initial KRnet $p_X^{(0)}(\mathbf{x}; \Theta_0^{(0)})$. The number of epochs is set to $N_e = 200$, and the maximum number of adaptivity iterations conducted for this problem is set to $N_{\text{adaptive}} = 5$. The learning rate for Adam optimizer is set to $\eta = 0.0001$, and the batch size is set to $m = 1000$. The initial training set C_0 is generated through the uniform distribution with range $[-5, 5]^2$, and the sample size is set to $|C_k| = 6 \times 10^4$ for each iteration step k for $k = 0, \dots, N_{\text{adaptive}}$. In addition, we take $L = 8$ affine coupling layers for both KRnet and real NVP, and two fully connected layers with $w = 48$ neurons for $\text{NN}_{[i]}$ (see (13)). For KRnet, we set $K = 2$ to focus on the effectiveness of the rotation layer and the nonlinear layer for this test problem. To assess the effectiveness of our ADDA-KR approach, we generate a validation data set $C_v = \{\mathbf{x}^{(i)}\}_{i=1}^{N_v}$, and compute the relative error defined by (35). The KL divergence is approximated by Monte Carlo integration

$$D_{KL}(p(\mathbf{x}) \| p_X(\mathbf{x}; \Theta)) \approx \frac{1}{N_v} \sum_{i=1}^{N_v} (\log p(\mathbf{x}^{(i)}) - \log p(\mathbf{x}^{(i)}; \Theta)), \quad (50)$$

where $\mathbf{x}^{(i)}$ is drawn from the exact solution $p(\mathbf{x})$, and the size of the validation data set is set to 3.2×10^5 such that the KL-divergence can be approximated well.

Figure 9 shows the relative error between the exact solution $p(\mathbf{x})$ and our ADDA-KR solution $p_X(\mathbf{x}; \Theta)$ at each adaptivity iteration step k . It is clear that, as the adaptivity iteration step increases, the relative error decreases quickly. In addition, it can be seen that as the number of epochs increases, the relative error decreases. Figure 10 shows the comparison between our ADDA-KR and ADDA-HH. From Figure 10(a), it can be seen that the relative error of

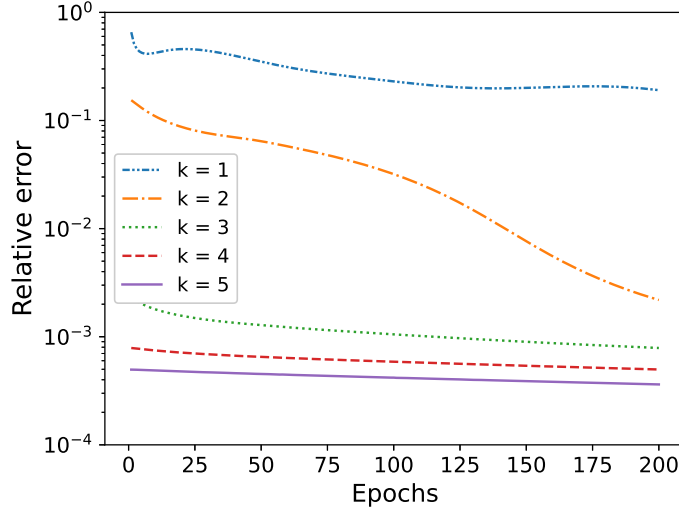


Figure 9: The relative error for ADDA-KR, two-dimensional bimodal test problem.

ADDA-KR is smaller than that of ADDA-HH at each adaptivity iteration step. Figure 10(b), Figure 10(c) and Figure 10(d) show the relative error decreases as the number of epochs increases, at adaptivity iteration steps $k = 1, 3, 5$ respectively. It can be seen that the relative error of ADDA-KR is clearly smaller than that of ADDA-HH for each value of epochs, except for the situations that the epoch number is smaller than 125 at the first adaptivity iteration in 10(b). Figure 11 shows the exact solution $p(\mathbf{x})$ and the ADDA-KR solution $p_X(\mathbf{x}; \Theta)$, where it can be seen that this bimodal distribution is well approximated by our ADDA-KR solution.

6.3. High-dimensional bimodal distributions (four-dimensional and eight-dimensional test problems)

In this part, we again consider the Fokker-Planck equation with two peaks (47) and set $\beta_1 = 0.55, \beta_2 = 0.45$. However, the dimensionality of the problem considered in this part is different from section 6.2. We here consider a four-dimensional ($d = 4$) problem and an eight-dimensional ($d = 8$) problem. The exact solution of (47) is a Gaussian mixture distribution (48). For $d = 4$, we set

$$\begin{aligned} \boldsymbol{\mu}_1 &= [-1, -1, -0.3, -0.3]^T, \boldsymbol{\mu}_2 = [2, 2, 0.6, 0.6]^T \\ \boldsymbol{\Sigma}'_1 &= \begin{bmatrix} \boldsymbol{\Sigma}_1 & \mathbf{0} \\ \mathbf{0} & 0.6\boldsymbol{\Sigma}_1 \end{bmatrix}, \quad \boldsymbol{\Sigma}'_2 = \begin{bmatrix} \boldsymbol{\Sigma}_2 & \mathbf{0} \\ \mathbf{0} & 0.6\boldsymbol{\Sigma}_2 \end{bmatrix}, \end{aligned} \quad (51)$$

where $\boldsymbol{\Sigma}_1$ and $\boldsymbol{\Sigma}_2$ are given in (49), and $\boldsymbol{\Sigma}'_1$ and $\boldsymbol{\Sigma}'_2$ are the covariance matrices of p_1 and p_2 for this test problem.

Similarly to the previous settings, we generate the initial parameters $\Theta_0^{(0)}$ with Glorot Gaussian initialization, and then construct the initial KRnet $p_X^{(0)}(\mathbf{x}; \Theta_0^{(0)})$. The number of epochs is set to $N_e = 1$, and the number of adaptivity iterations conducted for this problem is set to $N_{\text{adaptive}} = 16$. Here, KRnet is trained and sampled in an interleaved manner. That is for both the four-dimensional and the eight-dimensional test problems, samples C_k drawn at the k -th adaptivity iteration are immediately used for training KRnet at the $(k+1)$ -th iteration, while $p_X^{(k+1)}(\mathbf{x}; \Theta)$ is immediately used for sampling. The learning rate for Adam optimizer is set to $\eta = 0.0001$, and the batch size is set to $m = 500$. The

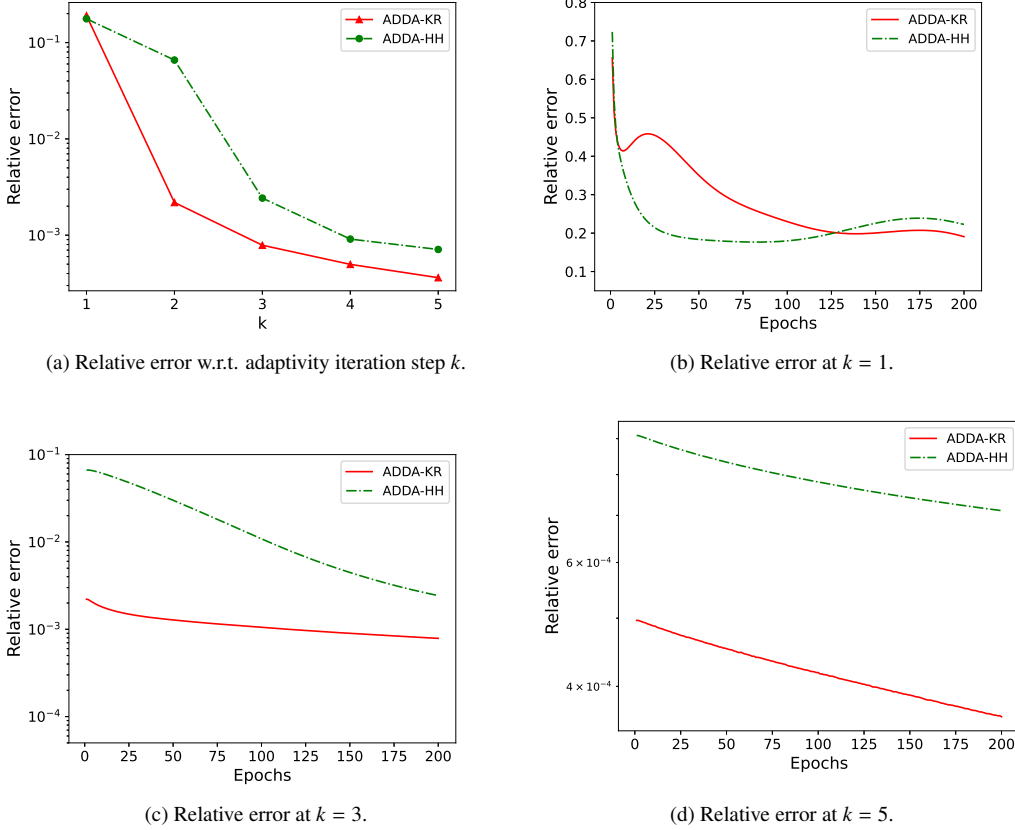


Figure 10: The relative error for ADDA-KR and ADDA-HH, two-dimensional bimodal test problem.

initial training set C_0 is generated through the uniform distribution with range $[-6, 6]^4$, and two cases of the collocation sample size are considered: one is 10^5 and the other is 2×10^5 . In addition, we take $L = 8$ affine coupling layers for KRnet, and $L = 16$ for real NVP. The architecture of $\text{NN}_{[i]}$ is the same as that shown in Figure 2 with $w = 120$. For KRnet, we set $K = 3$. The rotation layer and the nonlinear layer are turned on. To assess the accuracy of ADDA-KR, we again compute the relative error (35) between $p(\mathbf{x})$ and $p_X(\mathbf{x}; \Theta)$ using 3.2×10^5 validation samples drawn from the exact solution.

Figure 12 shows the relative error between $p(\mathbf{x})$ and $p_X(\mathbf{x}; \Theta)$ for ADDA-KR and ADDA-HH, where different numbers of collocation points are considered. From Figure 12(a), it can be seen that the relative error of ADDA-KR is smaller than that of ADDA-HH. From Figure 12(b) and Figure 12(c), as the number of epochs increases, the relative errors of ADDA-KR and ADDA-HH decrease quickly, while the relative errors of the uniform sampling strategies (Uniform-KR and Uniform-HH) decrease slowly. In addition, it can be seen that the relative error decreases as the number of training points increases from 10^5 to 2×10^5 for ADDA-KR, ADDA-HH, Uniform-KR and Uniform-HH.

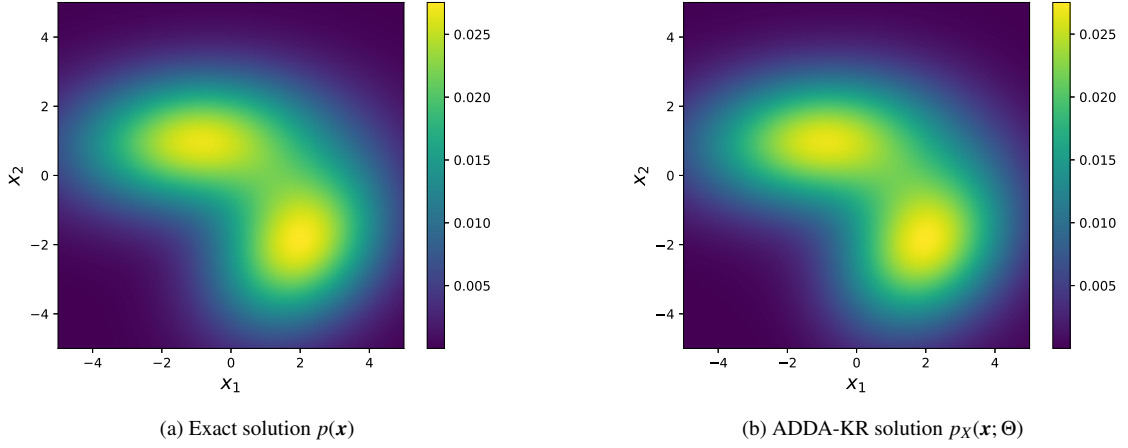


Figure 11: Solutions, two-dimensional bimodal modal test problem.

Finally, we consider an eight-dimensional bimodal distribution. For this problem, we set

$$\boldsymbol{\mu}_1 = [-1, -1, -0.3, -0.3, -0.4, -0.4, -1.6, -1.6]^T, \boldsymbol{\mu}_2 = [2, 2, 0.6, 0.6, 0.8, 0.8, 2.3, 2.3]^T$$

$$\tilde{\boldsymbol{\Sigma}}_1 = \begin{bmatrix} \boldsymbol{\Sigma}_1 & \mathbf{0} & \mathbf{0} & \mathbf{0} \\ \mathbf{0} & 0.6\boldsymbol{\Sigma}_1 & \mathbf{0} & \mathbf{0} \\ \mathbf{0} & \mathbf{0} & 0.8\boldsymbol{\Sigma}_1 & \mathbf{0} \\ \mathbf{0} & \mathbf{0} & \mathbf{0} & 1.2\boldsymbol{\Sigma}_1 \end{bmatrix}, \quad \tilde{\boldsymbol{\Sigma}}_2 = \begin{bmatrix} \boldsymbol{\Sigma}_2 & \mathbf{0} & \mathbf{0} & \mathbf{0} \\ \mathbf{0} & 0.6\boldsymbol{\Sigma}_2 & \mathbf{0} & \mathbf{0} \\ \mathbf{0} & \mathbf{0} & 0.8\boldsymbol{\Sigma}_2 & \mathbf{0} \\ \mathbf{0} & \mathbf{0} & \mathbf{0} & 1.2\boldsymbol{\Sigma}_2 \end{bmatrix}, \quad (52)$$

where $\boldsymbol{\Sigma}_1$ and $\boldsymbol{\Sigma}_2$ are given in (49), and $\tilde{\boldsymbol{\Sigma}}_1$ and $\tilde{\boldsymbol{\Sigma}}_2$ are the covariance matrices of p_1 and p_2 for this test problem.

Again, we generate the initial parameters $\Theta_0^{(0)}$ with Glorot Gaussian initialization, and then construct the initial KRnet $p_X^{(0)}(\mathbf{x}; \Theta_0^{(0)})$. The number of epochs is set to $N_e = 1$, and the maximum number of adaptivity iterations conducted for this problem is set to $N_{\text{adaptive}} = 120$. The learning rate for Adam optimizer is set to $\eta = 0.0001$, and the batch size is set to $m = 4000$. The initial training set C_0 is generated through the uniform distribution with range $[-6, 6]^8$, and two cases of the collocation sample size are considered: one is 3.2×10^5 and the other is 6.4×10^5 . In addition, we take $L = 10$ affine coupling layers for KR, and $L = 20$ for real NVP. The architecture of $\text{NN}_{[i]}$ is the same as that shown in Figure 2 with $w = 160$. For KRnet, we set $K = 3$. The rotation layer and the nonlinear layer are turned on. We again compute the relative error (35) using 3.2×10^5 validation samples drawn from the exact solution.

Figure 13 shows the relative error between $p(\mathbf{x})$ and $p_X(\mathbf{x}; \Theta)$ for ADDA-KR and ADDA-HH. From Figure 13(a), it can be seen that the relative error of ADDA-KR is smaller than that of ADDA-HH, when the number of epochs is larger than 60. From Figure 13(b) and Figure 13(c), as the number of epochs increases, the relative errors of ADDA-KR and ADDA-HH decrease quickly, while the relative errors of the uniform sampling strategies (Uniform-KR and Uniform-HH) decrease slowly. In addition, it can be seen that the relative error decreases as the number of collocation points increases from 3.2×10^5 to 6.4×10^5 for ADDA-KR, ADDA-HH, Uniform-KR and Uniform-HH.

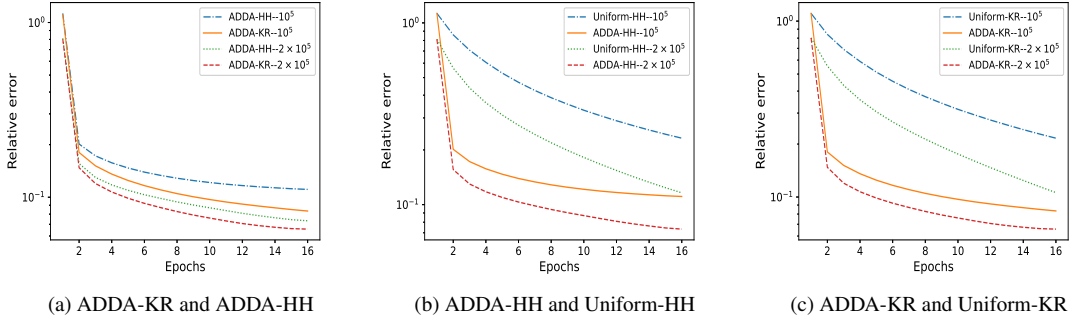


Figure 12: Relative errors, four-dimensional test problem.

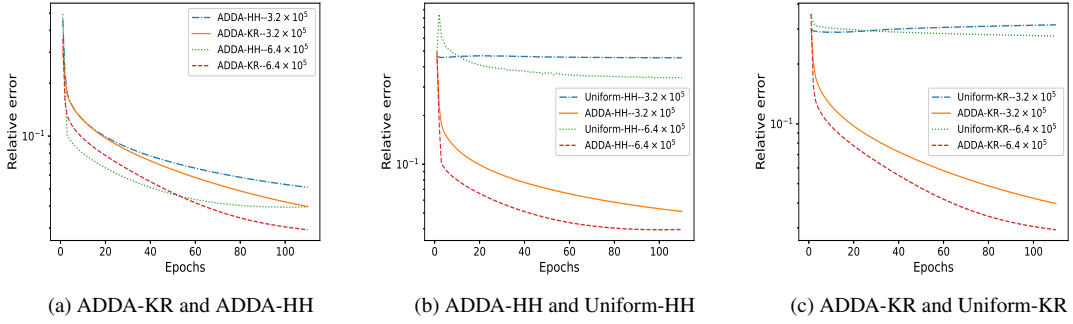


Figure 13: Relative errors, eight-dimensional test problem.

7. Conclusions

Conducting adaptivity is a fundamental concept of efficient numerical methods for the high-dimensional Fokker-Planck equation. With a focus on deep learning methods, we develop a novel adaptive deep density approximation strategy based on KRnet (ADDA-KR) in this work. Our KRnet, which is built on a new block-triangular structure and new layers including coupling, squeezing and rotation layers, gives a family of probability density functions, which can serve as solution candidates of the Fokker-Planck equation. We also show that KRnet is effective for estimating high-dimensional density functions in general. Our KRnet can efficiently generate collocation sample points, which lead to the overall closed loop our ADDA-KR strategy: train KRnet for the Fokker-Planck equation with current collocation points, and generate new collocation points using the KRnet for the next iteration. Compared with real NVP, which is a standard widely used generative model, numerical results show that our ADDA-KR gives much more accurate numerical solutions for the Fokker-Planck equation. However, ADDA-KR is currently limited to Fokker-Planck equations with dimension less than about 10, and current efforts are focused on dimension reduction for the high-dimensional variables. A possible solution for efficient dimension reduction is to decompose the spatial domain into small local subdomains through domain decomposition methods, and designing such strategies will be the focus of our future work.

Acknowledgments: K. Tang and Q. Liao are supported by the National Natural Science Foundation of China (No. 12071291) and the Science and Technology Commission of Shanghai Municipality (No. 20JC1414300), and X. Wan’s work was supported by the National Science Foundation under grant DMS-1913163.

References

- [1] H. Risken, Fokker-Planck-Kolmogorov equation, Springer, 1984.
- [2] S. Jin, B. Yan, A class of asymptotic-preserving schemes for the Fokker-Planck-Landau equation, *Journal of Computational Physics* 230 (2011) 6420–6437.
- [3] Y. Li, A data-driven method for the steady state of randomly perturbed dynamics, *Communications in Mathematical Sciences* 17 (2019) 1045–1059.
- [4] B. Spencer, L. Bergman, On the numerical solution of the Fokker-Planck equation for nonlinear stochastic systems, *Nonlinear Dynamics* 4 (4) (1993) 357–372.
- [5] H. C. Elman, D. J. Silvester, A. J. Wathen, Finite elements and fast iterative solvers: With applications in incompressible fluid dynamics, Oxford University Press, USA, 2014.
- [6] M. Dobson, Y. Li, J. Zhai, An efficient data-driven solver for Fokker-Planck equations: Algorithm and analysis (2019). [arXiv:1906.02600](https://arxiv.org/abs/1906.02600).
- [7] X. Chen, L. Yang, J. Duan, G. E. Karniadakis, Solving inverse stochastic problems from discrete particle observations using the Fokker-Planck equation and physics-informed neural networks (2020). [arXiv:2008.10653](https://arxiv.org/abs/2008.10653).
- [8] W. E, A proposal on machine learning via dynamical systems, *Communications in Mathematics and Statistics* 5 (1) (2017) 1–11.
- [9] W. E, B. Yu, The deep Ritz method: A deep learning-based numerical algorithm for solving variational problems, *Communications in Mathematics and Statistics* 6 (1) (2018) 1–12.
- [10] M. Raissi, P. Perdikaris, G. E. Karniadakis, Physics informed deep learning (part i): Data-driven solutions of nonlinear partial differential equations, arXiv preprint arXiv:1711.10561.
- [11] M. Raissi, P. Perdikaris, G. E. Karniadakis, Physics informed deep learning (part ii): Data-driven discovery of nonlinear partial differential equations, arXiv preprint arXiv:1711.10566.
- [12] M. Raissi, P. Perdikaris, G. E. Karniadakis, Physics-informed neural networks: A deep learning framework for solving forward and inverse problems involving nonlinear partial differential equations, *Journal of Computational Physics* 378 (2019) 686–707.
- [13] G. Pang, L. Lu, G. E. Karniadakis, fPINNs: Fractional physics-informed neural networks, *SIAM Journal on Scientific Computing* 41 (4) (2019) A2603–A2626.

[14] J. Sirignano, K. Spiliopoulos, DGM: A deep learning algorithm for solving partial differential equations, *Journal of Computational Physics* 375 (2018) 1339–1364.

[15] Y. Zhu, N. Zabaras, Bayesian deep convolutional encoder–decoder networks for surrogate modeling and uncertainty quantification, *Journal of Computational Physics* 366 (2018) 415–447.

[16] Y. Zhu, N. Zabaras, P.-S. Koutsourelakis, P. Perdikaris, Physics-constrained deep learning for high-dimensional surrogate modeling and uncertainty quantification without labeled data, *Journal of Computational Physics* 394 (2019) 56–81.

[17] K. Wu, D. Xiu, Numerical aspects for approximating governing equations using data, *Journal of Computational Physics* 384 (2019) 200–221.

[18] K. Wu, T. Qin, D. Xiu, Structure-preserving method for reconstructing unknown Hamiltonian systems from trajectory data, *SIAM Journal on Scientific Computing* 42 (6) (2020) A3704–A3729.

[19] K. Li, K. Tang, T. Wu, Q. Liao, D3M: A deep domain decomposition method for partial differential equations, *IEEE Access* 8 (2020) 5283–5294.

[20] A. D. Jagtap, E. Kharazmi, G. E. Karniadakis, Conservative physics-informed neural networks on discrete domains for conservation laws: Applications to forward and inverse problems, *Computer Methods in Applied Mechanics and Engineering* 365 (2020) 113028.

[21] S. Dong, Z. Li, Local extreme learning machines and domain decomposition for solving linear and nonlinear partial differential equations (2020). [arXiv:2012.02895](https://arxiv.org/abs/2012.02895).

[22] W. Li, X. Xiang, Y. Xu, Deep domain decomposition method: Elliptic problems, in: J. Lu, R. Ward (Eds.), *Proceedings of The First Mathematical and Scientific Machine Learning Conference*, Vol. 107 of *Proceedings of Machine Learning Research*, PMLR, Princeton University, Princeton, NJ, USA, 2020, pp. 269–286.

[23] A. Heinlein, A. Klawonn, M. Lanser, J. Weber, Combining machine learning and domain decomposition methods—a review, *Technical report*, Universität zu Köln (October 2020).

[24] E. Kharazmi, Z. Zhang, G. E. Karniadakis, hp-VPINNs: Variational physics-informed neural networks with domain decomposition, *Computer Methods in Applied Mechanics and Engineering* 374 (2021) 113547.

[25] H. Sheng, C. Yang, PFNN: A penalty-free neural network method for solving a class of second-order boundary-value problems on complex geometries, *Journal of Computational Physics* (2020) 110085.

[26] H. Gao, L. Sun, J.-X. Wang, Phygeonet: Physics-informed geometry-adaptive convolutional neural networks for solving parameterized steady-state PDEs on irregular domain, *Journal of Computational Physics* 428 (2021) 110079.

[27] D. Xiu, Numerical methods for stochastic computations: A spectral method approach, Princeton university press, 2010.

[28] D. Xiu, J. S. Hesthaven, High-order collocation methods for differential equations with random inputs, *SIAM Journal on Scientific Computing* 27 (3) (2005) 1118–1139.

[29] I. Babuška, F. Nobile, R. Tempone, A stochastic collocation method for elliptic partial differential equations with random input data, *SIAM Journal on Numerical Analysis* 45 (3) (2007) 1005–1034.

[30] J. Foo, X. Wan, G. E. Karniadakis, The multi-element probabilistic collocation method (ME-PCM): Error analysis and applications, *Journal of Computational Physics* 227 (22) (2008) 9572–9595.

[31] X. Ma, N. Zabaras, An adaptive hierarchical sparse grid collocation algorithm for the solution of stochastic differential equations, *Journal of Computational Physics* 228 (8) (2009) 3084–3113.

[32] A. Narayan, D. Xiu, Stochastic collocation methods on unstructured grids in high dimensions via interpolation, *SIAM Journal on Scientific Computing* 34 (3) (2012) A1729–A1752.

[33] H. Lei, X. Yang, B. Zheng, G. Lin, N. A. Baker, Constructing surrogate models of complex systems with enhanced sparsity: quantifying the influence of conformational uncertainty in biomolecular solvation, *Multiscale Modeling & Simulation* 13 (4) (2015) 1327–1353.

[34] D. W. Scott, Multivariate density estimation: theory, practice, and visualization, John Wiley & Sons, 2015.

[35] L. Dinh, J. Sohl-Dickstein, S. Bengio, Density estimation using real NVP (2016). [arXiv:1605.08803](https://arxiv.org/abs/1605.08803).

[36] D. P. Kingma, P. Dhariwal, Glow: Generative flow with invertible 1x1 convolutions, in: *Advances in Neural Information Processing Systems*, 2018, pp. 10215–10224.

[37] L. Zhang, W. E, L. Wang, Monge-Ampère flow for generative modeling (2018). [arXiv:1809.10188](https://arxiv.org/abs/1809.10188).

[38] T. Q. Chen, Y. Rubanova, J. Bettencourt, D. K. Duvenaud, Neural ordinary differential equations, in: *Advances in Neural Information Processing Systems*, 2018, pp. 6571–6583.

[39] G. Carlier, A. Galichon, F. Santambrogio, From Knothe’s transport to Brenier’s map and a continuation method for optimal transport, *SIAM Journal on Mathematical Analysis* 41 (6) (2010) 2554–2576.

[40] X. Wan, S. Wei, Coupling the reduced-order model and the generative model for an importance sampling estimator, *Journal of Computational Physics* 408 (2020) 109281.

[41] I. Goodfellow, J. Pouget-Abadie, M. Mirza, B. Xu, D. Warde-Farley, S. Ozair, A. Courville, Y. Bengio, Generative adversarial nets, in: *Advances in Neural Information Processing Systems*, 2014, pp. 2672–2680.

[42] D. P. Kingma, M. Welling, Auto-Encoding Variational Bayes, *stat* 1050 (2014) 1.

- [43] G. A. Pavliotis, Stochastic processes and applications: Diffusion processes, the Fokker-Planck and Langevin equations, Vol. 60, Springer, 2014.
- [44] K. Tang, X. Wan, Q. Liao, Deep density estimation via invertible block-triangular mapping, *Theoretical & Applied Mechanics Letters* 10 (2020) 143.
- [45] K. He, X. Zhang, S. Ren, J. Sun, Deep residual learning for image recognition, in: *Proceedings of the IEEE Conference on Computer Vision and Pattern Recognition*, 2016, pp. 770–778.
- [46] S. Ioffe, C. Szegedy, Batch normalization: Accelerating deep network training by reducing internal covariate shift (2015). [arXiv:1502.03167](https://arxiv.org/abs/1502.03167).
- [47] X. Glorot, A. Bordes, Y. Bengio, Deep sparse rectifier neural networks, in: *Proceedings of the Fourteenth International Conference on Artificial Intelligence and Statistics*, 2011, pp. 315–323.
- [48] D. P. Kingma, J. Ba, Adam: A method for stochastic optimization (2014). [arXiv:1412.6980](https://arxiv.org/abs/1412.6980).
- [49] G. Cybenko, Approximation by superpositions of a sigmoidal function, *Mathematics of Control, Signals and Systems* 2 (4) (1989) 303–314.
- [50] M. Leshno, V. Y. Lin, A. Pinkus, S. Schocken, Multilayer feedforward networks with a nonpolynomial activation function can approximate any function, *Neural Networks* 6 (6) (1993) 861–867.
- [51] Z. Lu, H. Pu, F. Wang, Z. Hu, L. Wang, The expressive power of neural networks: A view from the width, in: *Advances in Neural Information Processing Systems*, 2017, pp. 6231–6239.
- [52] L. Bottou, F. E. Curtis, J. Nocedal, Optimization methods for large-scale machine learning, *SIAM Review* 60 (2) (2018) 223–311.
- [53] X. Glorot, Y. Bengio, Understanding the difficulty of training deep feedforward neural networks, in: *Proceedings of the Thirteenth International Conference on Artificial Intelligence and Statistics*, 2010, pp. 249–256.